

# Chemical systematics of an intermediate spreading ridge: The Pacific-Antarctic Ridge between 56°S and 66°S

Ivan Vlastélic,<sup>1,2</sup> Laure Dosso,<sup>1</sup> Henri Bougault,<sup>3</sup> Daniel Aslanian,<sup>3</sup> Louis Géli,<sup>3</sup>  
Joël Etoubleau,<sup>3</sup> Marcel Bohn,<sup>1</sup> Jean-Louis Joron,<sup>4</sup> and Claire Bollinger<sup>1</sup>

**Abstract.** Axial bathymetry, major/trace elements, and isotopes suggest that the Pacific-Antarctic Ridge (PAR) between 56°S and 66°S is devoid of any hotspot influence. PAR (56–66°S) samples have in average lower  $^{87}\text{Sr}/^{86}\text{Sr}$  and  $^{143}\text{Nd}/^{144}\text{Nd}$  and higher  $^{206}\text{Pb}/^{204}\text{Pb}$  than northern Pacific mid-ocean ridge basalts (MORB), and also than MORB from the other oceans. The high variability of Pb isotopic ratios (compared to Sr and Nd) can be due to either a general high  $\mu$  (HIMU) (high U/Pb) affinity of the southern Pacific upper mantle or to a mantle event first recorded in time by Pb isotopes. Compiling the results of this study with those from the PAR between 53°S and 57°S gives a continuous view of mantle characteristics from south Pitman Fracture Zone (FZ) to Vacquier FZ, representing about 3000 km of spreading axis. The latitude of U dintsev FZ (56°S) is a limit between, to the north, a domain with large geochemical variations and, to the south, one with small variations. The spreading rate has intermediate values (54 mm/yr at 66°S to 74 mm/yr at 56°S) which increase along the PAR, while the axial morphology changes from valley to dome. The morphological transition is not recorded by the chemical properties of the ridge basalts nor by the inferred mantle temperature which displays few variations (30–40°C) along the PAR. Contrary to what is observed along the South-East Indian Ridge, PAR morphology appears to be controlled more by spreading rate rather than by mantle temperature. Much of the major and trace element variability results from segmentation control on the shallowest thermal structure of the mantle. The cold edge of a fracture zone seems to be more efficient when occurring in an axial dome context. It is expressed as an increase of the magnitude of the Transform Fault Effect along the valley-dome transition, resulting in a clear increase of trace element ratio variability (such as Nb/Zr). There is no strong evidence for the previously proposed southwestward asthenospheric flow in the area. However, this flow model could explain the intrasegment asymmetric patterns.

## 1. Introduction

Mid-ocean ridge sampling, at first concentrated in the most accessible regions, has reached in these last 10 years more remote ridges. Within the Pacific Ocean, samples recovered along the ridge axis south of 35°S were very few until a recent past: Ferguson and Klein [1993] have reported data from two dredges collected on the Pacific-Antarctic Ridge (PAR) at 64°S (on either side of Pitman Fracture Zone (FZ)) and from their geochemical study inferred a global homogeneity of the mantle underlying the Pacific Ocean spreading system. More recently, Castillo *et al.* [1998] have investigated the PAR between 53°S and 57°S and showed that to a first approximation, the southern Pacific mantle is similar in its composition to the northern one, but locally, it exhibits important heterogeneities. In this context, a geophysical and sampling cruise was organized in 1996 (Pacantarctic cruise, R/V *L'Atalante*, L. Géli and H. Bougault) to investigate the PAR from U dintsev Fracture Zone (FZ) at 145.1°W, 56°S, to south Pitman FZ at 173.8°W, 65.5°S, along a ridge crest distance of

1800 km (Figure 1). The main geological features of the area have been reported by Géli *et al.* [1997]. Isotopic data on ridge axis samples have been recently published by Vlastélic *et al.* [1999] where the mantle heterogeneity at the scale of the Pacific Ocean is discussed. We report here major/trace elements and complete Sr, Nd, Pb isotopic ratios. The following are the main debates relevant to this geochemical study:

1. As illustrated in Figure 1a, the PAR portion studied here is remote from any known hotspot. The closest ones are Louisville and Balleny hotspots (located ~1000 km from the extremities of our studied area), for which isotopic signatures are well defined and different [Cheng *et al.*, 1987; Green, 1992; Lanyon *et al.*, 1993]. Along the PAR segment located between U dintsev and Eltanin FZs, Castillo *et al.* [1998] reported enriched mantle influence which is likely to be due to the vicinity of the Hollister Ridge [Vlastélic *et al.*, 1998; Géli *et al.*, 1998]. This study may thus bring new constraints on the scale of mantle heterogeneity far away from hotspots.

2. Mainly based on morphological observations, a SW directed, along-axis asthenospheric flow has been proposed beneath the PAR [Marks and Stock, 1994; Sahabi *et al.*, 1996]. Between Vacquier and U dintsev FZs, Castillo *et al.* [1998] have recently identified subtle geochemical trends which could support this flow model. Here, the flow hypothesis can be tested by tracking southward the mantle heterogeneity revealed north of U dintsev FZ.

3. Axial morphology and spreading rate have been used to distinguish "cold" spreading centers, such as the Mid-Atlantic Ridge (MAR) (low spreading rate, axial valley) from "hot"

<sup>1</sup>UMR 6538, Domaines océaniques, IFREMER, Plouzané, France.

<sup>2</sup>Now at Max Planck-Institut für chemie, Mainz, Germany.

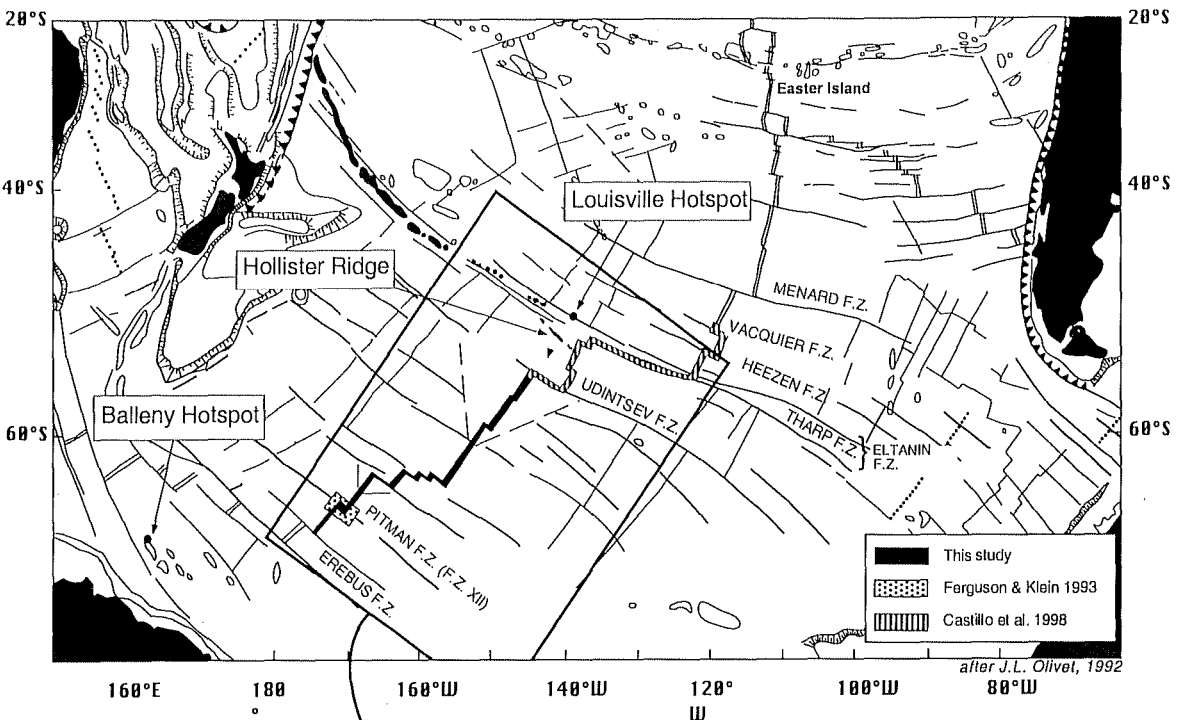
<sup>3</sup>IFREMER, Plouzané, France.

<sup>4</sup>Groupe des sciences de la Terre, Laboratoire Pierre Süe, Centre d'Etude Nucléaire de Saclay, Gif sur Yvette, France.

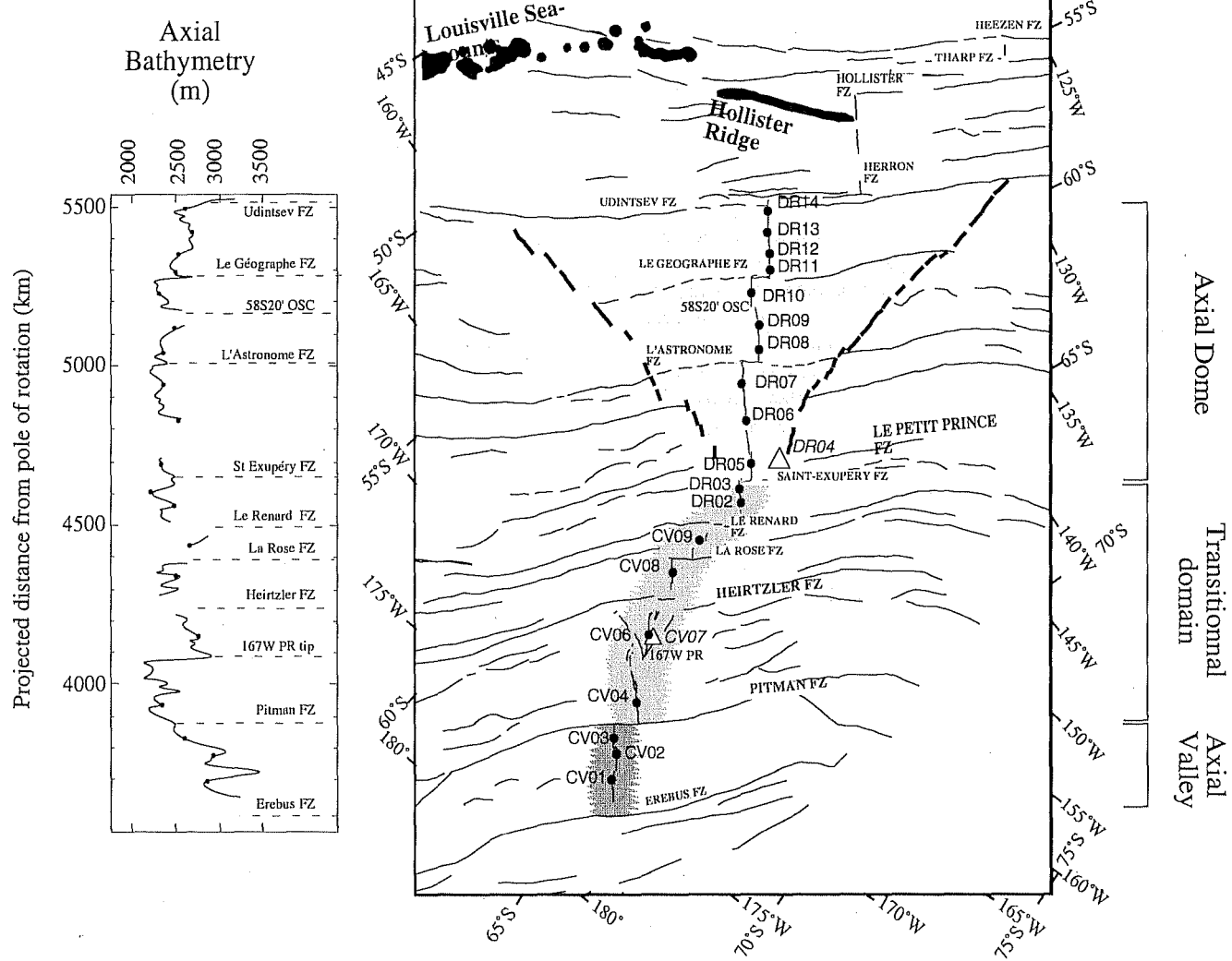
Copyright 2000 by the American Geophysical Union.

Paper number 1999JB900234.

0148-0227/00/1999JB900234\$09.00



b)



spreading centers, such the East Pacific Rise (EPR) (high spreading rate, axial dome). *Chen and Morgan* [1990a, b] predicted large effect of mantle temperature on the ridge morphology of slow and intermediate spreading ridges. Restricted to intermediate values (54–74 mm/yr), the PAR (56–66°S) spreading rate increases from SW toward NE, while the ridge morphology changes from valley to dome. The chemical data set presented here thus offers the possibility to test the relationship between ridge morphology and on one hand mantle temperature (inferred from petrological models) and on the other spreading rate.

## 2. Geological Setting

### 2.1. Previous Observations

From satellite gravity data it has been predicted [*Small and Sandwell*, 1989] that a transition from a dome-like to a valley-like axial topography occurs along the ridge axis, while the spreading rate is known to increase predictably with the distance from the Euler pole of rotation between the Antarctic and Pacific plates: from 54 mm/yr near 65°S up to 74 mm/yr at its intersection with U dintsev FZ, near 55°S [DeMets *et al.*, 1990]. Satellite gravity [*Sandwell *et al.**, 1994; *Smith and Sandwell*, 1997] also reveals a large V-shaped boundary (henceforth referred to as the V), extending over more than 1000 km south of U dintsev FZ and separating two domains: one of rough seafloor, with closely spaced, well-marked FZ as formed at slow spreading centers, and one of smooth seafloor comparable with the oceanic basins that have generally been formed at fast spreading centers (Figure 1b). *Sahabi *et al.** [1996] proposed that this V may reflect a southward propagation of the change in axial morphology south of U dintsev FZ during the last 30 Myr, at an average velocity of about 30 mm/yr.

### 2.2. Multibeam Observations

The multibeam survey of the area conducted during the Pacantarctic cruise revealed the following features. The PAR south of U dintsev FZ is divided into three sections of different

morphological signatures (Figure 1b) (H. Ondréas *et al.*, Variations in axial morphology along an intermediate spreading center: the Pacific-Antarctic Ridge between 56°S and 66°S, submitted to *Journal Geophysical Research*, 1999): (1) the southern section, between 65°30' S, 174°40' W and 64°40' S, 172°W (south Pitman FZ), has an axial valley-type of morphology similar to that observed at slow to intermediate spreading center, (2) the transitional domain, between Pitman and Saint Exupéry FZ, has an axial morphology which alternates from a flat axial dome to a shallow axial valley, and (3) the northern area, from Saint Exupéry FZ (62°S) to U dintsev FZ (56°S), has an axial dome morphology characteristic of fast spreading centers. The variation of ridge morphology is not clearly seen in the bathymetric profile in Figure 1b. Indeed, there is no pronounced long-wavelength bathymetric gradient: the axial depth displays relatively few variations within a 2200–3000 m range. Compared to the EPR north of 25°S (Easter Microplate) we note that (1) PAR (56–66°S) average axial depth is shallower (2450 m against 2850 m) and (2) the PAR segments which are characterized by a dome morphology lack the humped along-axis profile first mapped on the Pacific-Cocos EPR. This feature was first noted by *Lonsdale* [1994] between 35°S and 53°S and ascribed to less localized diapiric magma supply beneath the PAR.

## 3. Samples and Methods

Twenty sites were sampled at regular intervals (90 km) along the axis over a distance of 1800 km. The sampling tools used were the classical dredge (DR) and the rock core (CV) which allows a higher speed of sampling and better precision in location and depth but brings back smaller quantities of sample. Three samples were collected in the southern area (CV01 to CV03), seven samples in the transitional domain (CV04 to DR03), and 11 samples in the northern area (DR05 to DR14) (see Figure 1b). Sample CV07 was collected on a volcano (2500 to 1500 m) located in the ridge axis in the middle of the 65°40' S, 167°W propagating rift (termed 167W PR). Dredge DR04 was hauled on an off-axis seamount (Le Petit Prince seamount, 3000 to 500 m below sea level, 100 km off the ridge axis). All samples except DR04 are on-axis samples. All sampling operations brought back pillow lava or glassy material with a weak degree of alteration. A granodiorite was found in dredge 7 (DR07-4). In addition to pillow lava, DR04 brought back a basaltic pebble. Its shape and isotopic composition ( $^{206}\text{Pb}/^{204}\text{Pb} > 20$ ) suggest that it has been brought by an iceberg from the Antarctic continent. Its study is outside the scope of this work, and it is neither incorporated in tables nor in figures or discussion.

All analyzed samples were carefully selected by hand picking to avoid alteration effects. Major element analyses have been made either by microprobe (MP) on clean pieces of glass or by X-ray fluorescence (XRF, data in parentheses Table 1) on samples crushed in an agate mortar. Trace element analysis have been made by XRF (Zr, Nb, Y, V) and neutron activation analysis (NAA) (La, Sm). Analysis of Sr, Nd, Pb isotopic ratios were performed according to the procedure described by *Dosso *et al.** [1991]. All Pb measurements have been duplicated from different aliquots of the same powder. In order to remove seawater alteration effects, each powder was leached with 0.1 N HCl at 20°C for 30 min. Analytical uncertainties for isotopic ratios are better than  $\pm 0.000020$  for  $^{87}\text{Sr}/^{86}\text{Sr}$ ,  $\pm 0.000015$  for  $^{143}\text{Nd}/^{144}\text{Nd}$ ,  $\pm 0.005$  for  $^{206}\text{Pb}/^{204}\text{Pb}$  and  $^{207}\text{Pb}/^{204}\text{Pb}$ , and  $\pm 0.010$  for  $^{208}\text{Pb}/^{204}\text{Pb}$  (2σ mean). Major/trace element and isotope analysis of the samples are presented in Table 1.

**Figure 1.** (opposite) Map of the study area and sampling locations. (a) Map of the southern Pacific showing the location of the study area. Previous sampling are also shown: 53–57°S PAR, ruled pattern [*Castillo *et al.**, 1998] and 65°S PAR (two dredges in both sides of Pitman FZ), stippled pattern [*Ferguson and Klein*, 1993]. Position of Louisville and Balleny hotspots and the Hollister ridge are indicated. (b) Sampling locations of the Pacantarctic cruise. The names of the fracture zones (FZ), overlapping spreading center (OSC) and propagating rift (PR) are from *Géli *et al.** [1997]. The V-shaped dotted line separates one domain of rough seafloor (outside the V), with a high density of well-marked FZ from another with smooth seafloor (inside the V). This V-shaped structure (referred to as the V in the text), extending over more than 1000 km south U dintsev FZ, was revealed by satellite gravity [*Sandwell *et al.**, 1994]. Shaded areas indicate the variation in ridge morphology: dark shading for valley, medium shading for transitional domain, light shading for dome. Two sampling tools were used: CV for rock core and DR for dredge. Solid circles are for normal, on-axis samples. Small open triangle is for the on-ridge volcano (CV07). Large open triangle is for the off-axis volcano (DR04). The axial bathymetry (in m) is plotted according to the projected distance (in km) from the Pacific plate pole of rotation (101°E, 64.3°S).

Table 1. Major and Trace Element and Isotope Analyses for PAR (56-66°S) Samples

	Sample	Longitude, °S	Latitude, °W	Depth, m	Distance to pole, km	SiO <sub>2</sub> MP (XRF)	Al <sub>2</sub> O <sub>3</sub> MP (XRF)	FeO* MP (XRF)	MnO MP (XRF)	MgO MP (XRF)	CaO MP (XRF)	Na <sub>2</sub> O MP (XRF)	K <sub>2</sub> O MP (XRF)	TiO <sub>2</sub> MP (XRF)	Total
1	CV01-r	173.75	65.10	2863	3689	(49.08)	(17.35)	(8.93)	(0.15)	(8.20)	(12.22)	(1.87)	(0.05)	(1.00)	(98.85)
	CV01-g	173.75	65.10	2863	3689	49.78	15.70	9.79	0.18	8.45	11.71	2.49	0.04	1.10	99.22
	CV02-g	172.43	64.83	2936	3758	50.78	14.37	10.49	0.19	7.74	11.25	2.55	0.06	1.67	99.10
	CV03-r	171.88	64.53	2576	3798	(49.87)	(15.48)	(8.44)	(0.15)	(8.44)	(11.98)	(2.25)	(0.10)	(1.19)	(97.90)
Pitman FZ	CV03-g	171.88	64.53	2576	3798	50.70	15.53	8.60	0.16	8.57	11.91	2.53	0.08	1.20	99.27
2 Tip 167W	CV04-g	169.40	64.40	2340	3906	50.30	15.46	8.55	0.16	8.78	12.32	2.46	0.04	1.05	99.11
3	CV06-r	166.06	63.45	2755	4102	(49.23)	(17.51)	(8.06)	(0.14)	(8.06)	(12.59)	(1.77)	(0.05)	(1.05)	(98.46)
	CV06-g	166.06	63.45	2755	4102	50.44	15.37	9.31	0.17	8.51	12.01	2.50	0.04	1.23	99.59
	CV07-r	165.96	63.54	1603	4100	(50.52)	(14.30)	(9.77)	(0.18)	(7.82)	(12.27)	(2.27)	(0.06)	(1.34)	(98.53)
	CV07-g	165.96	63.54	1603	4100	51.06	14.50	9.80	0.19	7.88	12.03	2.71	0.04	1.31	99.52
La Rose FZ	CV08	162.44	62.77	2534	4292	(50.63)	(13.93)	(11.35)	(0.20)	(6.74)	(11.22)	(2.35)	(0.24)	(1.93)	(98.59)
4	CV09	159.61	62.66	2714	4408										
	DR02-g	156.54	62.64	2489	4522	50.97	14.33	9.98	0.18	7.65	11.53	2.87	0.08	1.58	99.17
	DR02-1	156.54	62.64	2489	4522	50.83	13.78	11.13	0.18	6.76	10.33	3.07	0.12	2.09	98.29
	DR02-3	156.54	62.64	2489	4522	50.88	14.32	10.01	0.17	7.46	11.42	2.77	0.08	1.64	98.77
	DR03-g	156.08	62.32	2219	4564	51.18	14.51	9.88	0.18	7.30	11.21	3.00	0.15	1.59	99.00
	DR03-1	156.08	62.32	2219	4564	51.17	14.56	9.80	0.20	7.32	11.19	3.09	0.15	1.59	99.06
St Exupéry FZ	DR03-2	156.08	62.32	2219	4564	50.98	14.52	9.95	0.18	7.33	11.26	3.04	0.15	1.58	99.00
Le Petit Prince seamount	DR04 ga	153.04	62.41	1587	4663	49.66	15.04	10.52	0.22	7.20	11.64	3.33	0.11	1.39	99.12
	DR04 gt	153.04	62.41	1587	4663	(49.13)	(15.71)	(10.08)	(0.18)	(7.25)	(11.83)	(2.87)	(0.12)	(1.35)	(98.52)
	DR04-1	153.04	62.41	1587	4663	(49.57)	(16.64)	(9.11)	(0.16)	(6.26)	(12.43)	(2.72)	(0.18)	(1.33)	(98.40)
Tip V	DR04-2r	153.04	62.41	1587	4663	(48.94)	(15.28)	(10.77)	(0.74)	(7.09)	(11.51)	(2.44)	(0.23)	(1.36)	(98.36)
5	DR05-1g	154.54	62.00	2344	4645	51.00	15.45	8.42	0.15	8.33	12.01	2.82	0.09	1.19	99.47
	DR05-2	154.54	62.00	2344	4645	50.62	15.76	8.37	0.16	8.73	11.94	2.72	0.11	1.15	99.57
	DR05-3	154.54	62.00	2344	4645	50.79	15.51	8.32	0.16	8.32	12.02	2.68	0.08	1.16	99.06
	DR05-r	154.54	62.00	2344	4645	(49.96)	(15.24)	(8.52)	(0.15)	(8.29)	(12.13)	(2.70)	(0.11)	(1.21)	(98.31)
	DR06-g	153.21	60.94	2527	4780	50.99	13.99	11.20	0.20	6.93	10.58	2.86	0.12	2.02	98.89
	DR06-1r	153.21	60.94	2527	4780	(50.15)	(14.07)	(11.35)	(0.19)	(7.05)	(10.84)	(2.50)	(0.14)	(2.06)	(98.35)
	DR06-2	153.21	60.94	2527	4780	50.43	13.95	10.96	0.19	6.98	10.46	2.86	0.12	1.96	97.92
	DR07-1g	152.08	60.00	2362	4900	50.75	14.43	10.70	0.22	6.83	10.58	3.03	0.19	1.94	98.65
	DR07-2g	152.08	60.00	2362	4900	50.83	14.43	10.52	0.18	7.35	11.29	2.91	0.12	1.69	99.32
	DR07-3	152.08	60.00	2362	4900	50.43	14.17	10.22	0.19	7.24	11.11	2.93	0.12	1.70	98.12
L'Astronome FZ	DR07-4	152.08	60.00	2362	4900	(52.20)	(17.89)	(6.65)	(0.14)	(6.59)	(10.77)	(2.81)	(0.68)	(1.03)	(98.76)
6	DR08-1	150.02	59.50	2365	5016	50.80	13.85	10.99	0.20	6.95	11.06	2.94	0.10	1.88	98.78
	DR08-2	150.02	59.50	2365	5016	50.95	13.79	11.21	0.21	6.77	10.96	2.95	0.11	1.91	98.85
	DR08-3	150.02	59.50	2365	5016	(50.34)	(13.86)	(11.07)	(0.19)	(7.00)	(11.43)	(2.33)	(0.13)	(1.90)	(98.25)
	DR09-g	149.14	58.85	2484	5104	50.75	13.42	12.15	0.22	6.36	10.44	3.09	0.12	2.20	98.76
	DR09-1	149.14	58.85	2484	5104	(49.59)	(13.31)	(12.03)	(0.21)	(6.47)	(10.90)	(2.26)	(0.20)	(2.20)	(97.17)
	DR09-2	149.14	58.85	2484	5104	(49.91)	(13.38)	(11.81)	(0.20)	(6.31)	(10.84)	(2.49)	(0.20)	(2.20)	(97.34)
	DR10-1g	148.50	57.89	2319	5211	53.79	14.10	10.77	0.21	4.83	8.59	3.43	0.48	1.73	97.92
	DR10-2g	148.50	57.89	2319	5211	51.46	14.10	10.87	0.20	6.22	10.36	3.37	0.25	1.75	98.60
Le Géographie FZ	DR10-3	148.50	57.89	2319	5211	(50.29)	(14.29)	(10.39)	(0.18)	(7.17)	(11.58)	(2.53)	(0.23)	(1.71)	(98.37)
7	DR11-1g	146.80	57.63	2500	5294	50.21	14.32	9.25	0.17	7.33	11.34	2.70	0.06	1.31	96.69
	DR11-2g	146.80	57.63	2500	5294	51.09	14.55	9.74	0.19	7.55	11.87	2.75	0.06	1.39	99.19
	DR11-3	146.80	57.63	2500	5294	(50.36)	(14.39)	(9.75)	(0.18)	(7.81)	(12.07)	(2.02)	(0.09)	(1.41)	(98.08)
	DR12-1g	146.29	57.18	2539	5353	50.94	15.62	8.49	0.15	8.85	12.31	2.32	0.03	1.03	99.74
	DR12-2g	146.29	57.18	2539	5353	50.90	15.55	8.70	0.16	8.76	12.32	2.30	0.03	1.04	99.78
	DR12-3g	146.29	57.18	2539	5353	50.59	13.73	11.12	0.20	6.80	10.77	2.74	0.10	2.10	98.16
	DR12-3r	146.29	57.18	2539	5353	50.73	13.78	11.40	0.19	6.89	10.88	2.72	0.10	2.13	98.80
	DR13-1g	145.74	56.57	2674	5428	50.37	14.60	10.89	0.18	7.38	10.76	2.82	0.09	1.64	98.73
	DR13-2g	145.74	56.57	2674	5428	50.50	14.52	11.01	0.19	7.42	10.73	2.85	0.09	1.65	98.96
	DR13-3	145.74	56.57	2674	5428	(49.91)	(14.45)	(11.24)	(0.19)	(7.44)	(10.97)	(2.51)	(0.10)	(1.70)	(98.51)
	DR14-1	145.09	56.00	2617	5503	(50.60)	(14.97)	(9.09)	(0.16)	(8.24)	(12.26)	(2.08)	(0.13)	(1.15)	(98.68)
	DR14-2	145.09	56.00	2617	5503	50.83	15.15	9.01	0.18	8.02	11.97	2.74	0.09	1.17	99.16
	DR14-3	145.09	56.00	2617	5503	50.98	14.88	9.02	0.17	7.97	12.11	2.60	0.12	1.13	98.99
	DR14-4	145.09	56.00	2617	5503	51.09	14.93	9.14	0.17	7.99	12.16	2.61	0.12	1.13	99.34
Udintsev FZ	DR14-5	145.09	56.00	2617	5503	51.09	15.03	9.11	0.18	7.99	12.14	2.61	0.12	1.13	99.41

Distances to pole refer to the pole of rotation of the Pacific plate (101°E; 64.3°S). All major element concentrations are expressed in wt %. FeO\* is total iron expressed as FeO. All trace element concentrations expressed in ppm. MP, microprobe; XRF, X-ray fluorescence (in parentheses); NAA, neutron activation analysis; isotope ratios have been done on lightly leached powders (0.1 N HCl); g, glass; r, rock; ga, altered glass; gt, selected unaltered glass.

Table 1. (continued)

	Sample	Total	Zr (XRF)	Nb (XRF)	La NAA	Sm NAA	Y (XRF)	V (XRF)	$^{87}\text{Sr}/^{86}\text{Sr}^a$	$^{143}\text{Nd}/^{144}\text{Nd}^b$	$^{206}\text{Pb}/^{204}\text{Pb}^c$	$^{207}\text{Pb}/^{204}\text{Pb}^c$	$^{208}\text{Pb}/^{204}\text{Pb}^c$
1	CV01-r	(98.85)	(47)	(1.27)	1.47	2.09	(20.6)	(198)	0.702551	0.513153	18.408	15.562	38.154
	CV01-g	99.22	(53)	(1.43)	1.88	2.42	(21.7)	(207)	0.702597	0.513124	18.772	15.606	38.633
	CV02-g	99.10	(105)	(2.13)	3.01	4.03	(36.6)	(334)	0.702568	0.513135	18.395	15.491	37.916
	CV03-r	(97.90)	(80)	(2.40)	2.88	3.01	(23.5)	(250)	0.702423	0.513109	18.470	15.497	37.968
Pitman FZ	CV03-g	99.27	(77)	(2.21)	2.88	2.83	(23.9)	(255)	0.702406	0.513117	18.497	15.498	38.093
2 Tip 167W	CV04-g	99.11	(64)	(1.03)	1.97	2.51	(23.1)	(251)	0.702512	0.513144	18.152	15.453	37.596
3	CV06-r	(98.46)	(60)	(0.90)	1.69	2.37	(22.5)	(225)	0.702362	0.513128	18.358	15.498	37.899
	CV06-g	99.59	(56)	(0.80)	1.66	2.34	(21.0)	(214)	0.702397	0.513129	18.366	15.493	37.894
	CV07-r	(98.53)	(79)	(1.08)	2.35	3.14	(28.1)	(292)	0.702402	0.513151	18.261	15.505	37.889
La Rose FZ	CV07-g	99.52	(82)	(1.50)	4.81	3.53	(27.9)	(291)	0.702778	0.513002	18.558	15.578	38.376
4	CV08	(98.59)	(127)	(3.84)	4.83	4.56	(37.0)	(353)	0.702419	0.513112	18.464	15.496	37.974
	CV09								0.702370	0.513110	18.287	15.610	38.170
	DR02-g	99.17	(107)	(2.43)	3.43	3.97	(32.7)	(300)	0.702335	0.513141	18.295	15.488	37.807
	DR02-1	98.29	(158)	(4.26)	5.77	5.35	(44.0)	(366)	0.702362	0.513147	18.354	15.481	37.838
	DR02-3	98.77	(112)	(2.64)	3.65	4.08	(34.9)	(315)					
	DR03-g	99.00	(118)	(4.91)	5.23	3.91	(32.1)	(292)					
St Exupéry FZ	DR03-1	99.06	(117)	(5.00)	5.58	4.09	(31.9)	(302)	0.702421	0.513107	18.493	15.500	38.013
	DR03-2	99.00	(120)	(4.90)	5.57	4.13	(31.9)	(305)	0.702439	0.513106	18.493	15.495	37.993
Le Petit Prince seamount	DR04 ga	99.12	(90)	(3.63)	4.30	3.29	(25.8)	(227)					
	DR04 gt	(98.52)			3.52	3.41		(251)	0.702649	0.513091	18.716	15.608	38.630
	DR04-1	(98.40)	(88)	(3.30)	3.38	3.19	(27.8)	(250)					
Tip V	DR04-2r	(98.36)	(112)	(5.66)	8.11	4.20	(27.9)	(251)	0.703212	0.512879	18.807	15.664	38.854
5	DR05-1g	99.47	(86)	(3.43)	3.77	3.08	(25.4)	(243)	0.702407	0.513132	18.491	15.507	37.998
	DR05-2	99.57	(80)	(3.89)	3.78	2.92	(23.8)	(242)					
	DR05-3	99.06	(80)	(3.01)	3.05	2.99	(24.0)	(249)	0.702435	0.513138	18.495	15.501	37.983
	DR05-r	(98.31)	(80)	(2.86)	3.11	2.86	(24.4)	(242)	0.702455	0.513122	18.483	15.494	37.953
	DR06-g	98.89	(140)	(3.65)	4.58	4.67	(42.1)	(366)	0.702502	0.513126	18.504	15.505	37.987
	DR06-1r	(98.35)	(141)	(3.88)	4.76	5.10	(41.9)	(363)					
	DR06-2	97.92	(141)	(3.62)	4.71	4.81	(42.2)	(365)	0.702389	0.513113	18.496	15.501	37.970
	DR07-1g	98.65	(148)	(5.77)	6.11	5.02	(40.0)	(344)	0.702472	0.513099	18.632	15.498	38.074
	DR07-2g	99.32	(113)	(3.44)	4.36	4.31	(33.1)	(323)	0.702454	0.513098	18.637	15.527	38.154
L'Astronome FZ	DR07-3	98.12	(121)	(3.85)	4.57	4.23	(35.3)	(326)	0.702428	0.513090	18.620	15.505	38.086
6	DR07-4	(98.76)	(138)	(6.78)	16.35	5.49	(20.3)	(141)	0.703442	0.512957	18.820	15.580	38.550
Le Géographe FZ	DR08-1	98.78	(134)	(2.70)	4.08	4.49	(37.8)	(335)					
	DR08-2	98.85	(132)	(2.57)	4.01	4.40	(37.0)	(344)	0.702388	0.513110	18.412	15.489	37.885
	DR08-3	(98.25)	(135)	(2.54)	4.14	4.53	(37.6)	(335)	0.702376	0.513113	18.404	15.483	37.858
	DR09-g	98.76	(153)	(3.36)	4.70	5.27	(44.4)	(377)	0.702467	0.513120	18.422	15.503	37.953
	DR09-1	(97.17)	(152)	(3.46)	4.86	5.35	(44.2)	(381)	0.702372	0.513112	18.382	15.483	37.882
	DR09-2	(97.34)	(151)	(3.37)	4.74	5.19	(43.4)	(382)					
	DR10-1g	97.92	(355)	(13.62)	14.27	9.50	(71.1)	(227)	0.702473	0.513112	18.435	15.510	37.968
	DR10-2g	98.60	(190)	(7.97)	8.14	6.34	(46.9)	(280)					
Le Géographe FZ	DR10-3	(98.37)	(122)	(5.98)	5.52	4.24	(32.6)	(302)	0.702470	0.513127	18.413	15.498	37.927
7	DR11-1g	96.69	(89)	(1.93)	3.11	3.45	(28.9)	(294)	0.702435	0.513125	18.401	15.494	37.862
	DR11-2g	99.19	(91)	(1.97)	2.90	3.42	(29.3)	(293)					
	DR11-3	(98.08)	(88)	(1.77)	3.10	3.42	(27.7)	(300)	0.702469	0.513129	18.404	15.499	38.072
	DR12-1g	99.74	(62)	(0.82)	1.87	2.58	(23.9)	(248)	0.702310	0.513150	18.015	15.473	37.506
	DR12-2g	99.78	(62)	(0.82)	1.80	2.56	(24.1)	(254)					
	DR12-3g	98.16	(141)	(3.39)	4.32	5.03	(43.5)	(373)	0.702375	0.513146	18.202	15.481	37.690
	DR12-3r	98.80	(140)	(3.31)	4.35	4.95	(42.8)	(363)	0.702395	0.513170	18.204	15.485	37.699
	DR13-1g	98.73	(109)	(2.86)	3.51	4.09	(35.2)	(315)					
	DR13-2g	98.96	(107)	(2.86)	3.79	3.92	(35.2)	(309)	0.702556	0.513142	18.500	15.497	37.966
	DR13-3	(98.51)	(108)	(2.84)	3.53	4.07	(35.9)	(313)	0.702570	0.513145	18.514	15.509	38.008
	DR14-1	(98.68)	(74)	(3.72)	3.69	2.80	(23.8)	(243)					
	DR14-2	99.16	(77)	(2.93)	3.44	2.89	(23.6)	(247)	0.702538	0.513138	18.512	15.511	38.209
	DR14-3	98.99	(73)	(3.78)	3.71	2.82	(22.7)	(243)	0.702530	0.513102	18.755	15.523	38.386
Udintsev FZ	DR14-4	99.34	(71)	(3.76)	3.77	2.80	(22.4)	(248)	0.702557	0.513131	18.774	15.512	38.382
	DR14-5	99.41	(73)	(3.58)	3.79	2.86	(22.5)	(248)					

<sup>a</sup>Analytical uncertainties for Pb isotopic ratios are approximately  $\pm 0.005$  for  $^{206}\text{Pb}/^{204}\text{Pb}$  and  $^{207}\text{Pb}/^{204}\text{Pb}$  and  $\pm 0.01$  for  $^{208}\text{Pb}/^{204}\text{Pb}$ . Total procedural blanks are  $< 0.3$  ng for Pb. Isotopic composition normalized to  $^{88}\text{Sr}/^{86}\text{Sr} = 0.1194$  and referred to NBS987 =  $0.710260 \pm 0.00002$ .

<sup>b</sup>Isotopic composition normalized to  $^{146}\text{Nd}/^{144}\text{Nd} = 0.7219$  and referred to La Jolla Nd =  $0.511852 \pm 0.000010$ .

<sup>c</sup>Isotopic data were corrected for instrumental mass fractionation by applying a discrimination factor determined by multiple analysis of NBS981; all Pb isotopic ratios are relative to NBS981;  $^{206}\text{Pb}/^{204}\text{Pb} = 16.9373$ ,  $^{207}\text{Pb}/^{204}\text{Pb} = 15.4925$ , and  $^{208}\text{Pb}/^{204}\text{Pb} = 36.7054$ .

**Table 2.** Average Major Element Amounts and Isotopic Ratios of the PAR (56-66°S) and EPR (16°N-23°S)

PAR 56-66°S					EPR 16°N-23°S			
	Mean Value, m	n	2σ	σ/m	Mean Value, m	n	2σ	σ/m
SiO <sub>2</sub>	50.638	56	1.349	0.013	50.378	159	1.862	0.018
Al <sub>2</sub> O <sub>3</sub>	14.712	56	1.845	0.062	14.775	159	2.205	0.071
FeO*	9.958	56	2.312	0.116	10.623	159	3.054	0.143
MnO	0.180	56	0.040	0.111	0.187	159	0.077	0.207
MgO	7.542	56	1.568	0.103	7.368	159	2.069	0.140
CaO	11.436	56	1.444	0.063	11.394	159	1.753	0.076
Na <sub>2</sub> O	2.659	56	0.648	0.122	2.782	159	0.678	0.121
K <sub>2</sub> O	0.123	56	0.210	0.852	0.134	159	0.209	0.782
TiO <sub>2</sub>	1.528	56	0.732	0.239	1.735	159	0.836	0.241
<sup>87</sup> Sr/ <sup>86</sup> Sr	0.702449	44	0.00017	0.00012	0.702577	135	0.00025	0.00018
<sup>143</sup> Nd/ <sup>144</sup> Nd	0.513123	44	0.00005	0.00005	0.513141	119	0.00009	0.00009
<sup>206</sup> Pb/ <sup>204</sup> Pb	18.435	44	0.303	0.00823	18.336	109	0.395	0.01080
<sup>207</sup> Pb/ <sup>204</sup> Pb	15.502	44	0.066	0.00214	15.482	109	0.066	0.00214
<sup>208</sup> Pb/ <sup>204</sup> Pb	37.971	44	0.423	0.00557	37.820	109	0.477	0.00632

EPR data sources are Prinzhofer et al. [1989], Sinton et al. [1991], Niu et al. [1996], Bach et al. [1994] for major elements and Sun [1980], Cohen et al. [1980], White and Hofmann [1982], Cohen and O'Nions [1982], Hamelin et al. [1984], Zindler et al. [1984], Macdougall and Lugmair [1986], White et al. [1987], Ito et al. [1987], Prinzhofer et al. [1989], Mahoney et al. [1994], Bach et al. [1994], Niu et al. [1996], and Schiano et al. [1997] for isotopic ratios. PAR data source (major elements and isotopes) is Ferguson and Klein, [1993] and this study. Only on-ridge samples are considered. FeO\* is total iron expressed as FeO. All major element concentrations in wt %. All isotopic data have been renormalized to equivalent standard values. Sr isotopic compositions are relative to NBS987 = 0.71025 or Eimer and Amend = 0.70803. Nd isotopic compositions are relative to La Jolla Nd = 0.511852 or BCR1 = 0.512627. Pb isotopic compositions are relative to NBS981: <sup>206</sup>Pb/<sup>204</sup>Pb = 16.9373, <sup>207</sup>Pb/<sup>204</sup>Pb = 15.4925, and <sup>208</sup>Pb/<sup>204</sup>Pb = 36.7054.

## 4. Analytical Results

### 4.1. Major and Trace Elements

Major element compositions of all on-axis samples analyzed (except DR07-4) are typical of normal mid-ocean ridge basalt (NMORB). Except for sample DR10-1g which has undergone extensive low-pressure differentiation ( $MgO = 4.83$  wt %), the samples range from relatively primitive ( $MgO = 8.78$  wt %) to moderately evolved ( $MgO = 6.22$  wt %) compositions. Compared to PAR (56-66°S) NMORB and based on microprobe analysis (except DR10-1g,  $n = 35$ ), the near-ridge volcano sample (DR04-g) has lower  $SiO_2$  and higher  $Na_2O$ , whereas the on-ridge volcano sample (CV07-g) has similar major element amounts. Ferguson and Klein [1993] noted that samples from the PAR (64°S) are remarkably similar in major element composition to NMORB samples from the northern EPR. However, they noted that PAR samples (six analyses,  $SiO_2 = 50.44 \pm 0.57$ ) have higher  $SiO_2$ . A comparison between PAR (56-66°S,  $n = 56$ ) and EPR (16°N-23°S,  $n = 159$ ) major element concentrations is presented in Table 2. The deepest part of the EPR (between 16°N and 23°S, which is on average 400 m deeper than the PAR) was selected because Klein and Langmuir [1987] have shown that there is a relationship on a global scale between major element chemistry and ridge depth. Note that both portions of ridges are unaffected by any hotspot. Table 2 indicates slight differences in major element concentrations between the two areas. However, taking into account the large dispersion of data (see  $2\sigma$ ) and the fact that the samples were analyzed by different techniques, it would be hazardous to ascribe a difference in major element concentrations, between the two areas.

All PAR samples are depleted ( $(La/Sm)_N$  from 0.42 to 0.89) except for the enriched granodiorite sample DR07-4 which has a  $(La/Sm)_N$  of 1.77. Among seamount samples, only sample DR04-2-r is enriched with a  $(La/Sm)_N$  of 1.15. A remarkable feature is the large range of trace element concentrations in dredge 10 (Zr

ranges from 122 to 355 ppm), whereas Sr and Nd (and to a lesser extent Pb) isotopic ratios display very few variations (see Table 1). The large variation in  $MgO$  content of these samples points out to crystal fractionation as a likely cause of this observation. Because of the well-known similarity of behavior between, on one hand, La and Nb and, on the other hand, Sm and Zr,  $(Nb/Zr)_N$  can be used in place of  $(La/Sm)_N$  to indicate the shape of extended rare earth element (XREE) patterns. When  $(La/Sm)_N$  is not given in the literature,  $(Nb/Zr)_N$ , when available, is used instead to compare XREE patterns. Within the depleted samples, trace element concentrations display variations ( $(Nb/Zr)_N$  from 0.146 to 0.584) which encompass the 13-23°S EPR range ( $(Nb/Zr)_N$  from 0.170 to 0.515) [Mahoney et al., 1994]. We note that 56-66°S PAR includes many samples having  $(Nb/Zr)_N > 0.35$  (especially in the northern part of our study area), whereas such values are very rarely measured along the 13-23°S EPR portion. Samples from the seamounts display  $(Nb/Zr)_N$  values which are within the range of normal ridge samples (0.202 for CV07-g, from 0.414 to 0.558 for DR04 samples).

### 4.2. Isotopes

Except for samples from the seamounts and sample DR07-4, isotopic ratios range only from 0.702310 to 0.702597 for  $^{87}Sr/^{86}Sr$ , from 0.513090 to 0.513170 for  $^{143}Nd/^{144}Nd$  and from 18.015 to 18.774 for  $^{206}Pb/^{204}Pb$  (see Figure 2). PAR data generally fall within the Pacific MORB fields (Figures 2a-2d). A more detailed study of Pacific MORB [Vlastelic et al., 1999] shows that PAR data fall on the low Sr (Nd-Sr plot) and high Pb (Sr-Pb plot) arrays, leading to the identification of two large-scale provinces within the Pacific Ocean. As shown in Table 2, 56-66°S PAR samples display in average lower  $^{87}Sr/^{86}Sr$  and  $^{143}Nd/^{144}Nd$  with higher  $^{206}Pb/^{204}Pb$  than EPR samples between 16°N and 23°S. When a ridge section of similar length is considered, such as the 13-23°S EPR, 56-66°S PAR samples display slightly less Nd and Sr variations but slightly more Pb

**Figure 2.** (opposite) Isotope plots: (a)  $^{143}Nd/^{144}Nd$  versus  $^{87}Sr/^{86}Sr$ , (b)  $^{87}Sr/^{86}Sr$  versus  $^{206}Pb/^{204}Pb$ , (c)  $^{207}Pb/^{204}Pb$  versus  $^{206}Pb/^{204}Pb$ , and (d)  $^{208}Pb/^{204}Pb$  versus  $^{206}Pb/^{204}Pb$ . PAR data are shown by solid circles. Seamounts data are shown by triangles (large open triangle labeled "S" by triangles (large open triangle labeled "S" for the off-axis seamount DR04, small open triangle labeled "s" for the on-axis seamount CV07). Fields for MORB isotope data from Atlantic, Pacific and Indian are shown for comparison. References for MORB fields are: Schilling [1973]; Hart et al. [1973]; Sun et al. [1975]; Dickey et al. [1977]; White and Schilling [1978]; Dupré and Allègre [1980]; Machado et al. [1982]; Le Roex et al. [1985]; Hanan et al. [1986]; Le Roex et al. [1987]; Shirey et al. [1987]; Castillo and Batiza [1989]; Mertz et al. [1991]; Dosso et al. [1991, 1993]; Frey et al. [1993]; Schilling et al. [1994]; Fontignie and Schilling [1996]; Graham et al. [1996]; Mertz and Haase [1997]; and Yu et al. [1997] and unpublished data for Atlantic Ocean. Church and Tatsumoto [1975]; Vidal and Clauer [1981]; Verma et al. [1983]; Zindler et al. [1984]; Macdougall and Lugmair [1985, 1986]; White et al. [1987]; Hegner and Tatsumoto [1987]; Prinzhofer et al. [1989]; Hanan and Schilling [1989]; Fontignie and Schilling [1991]; Ferguson and Klein [1993]; Mahoney et al. [1994]; Bach et al. [1994, 1996]; Niu et al. [1996]; Castillo et al. [1998] for Pacific ocean. Dupré and Allègre, [1983]; Le Roex et al. [1983]; Hamelin and Allègre [1985]; Hamelin et al. [1986]; Price et al. [1986]; Michard et al. [1986]; Dosso et al. [1988]; Mahoney et al. [1989, 1992]; Le Roex et al. [1992] for Indian ocean. General papers used are: Tatsumoto [1978]; Sun et al. [1979]; Sun [1980]; Cohen et al. [1980]; Dupré et al. [1981]; White and Hofmann [1982]; Cohen and O'Nions [1982]; Hamelin et al. [1984]; Ito et al. [1987]; Klein et al. [1988]; Pyle et al. [1992]; Schiano et al. [1997]; Kurz et al. [1998]. Note that papers from the Australian-Antarctic Discordance (AAD) belong to the general papers because they report both Indian-type isotopes (west AAD) and Pacific-type isotopes (east AAD). All data have been renormalized to equivalent standards values. Sr isotopic compositions are relative to NBS987 = 0.711025 or E&A = 0.70803. Nd isotopic compositions are relative to La Jolla Nd = 0.511852 or BCRI = 0.512640. Pb isotopic compositions relative to NBS981;  $^{206}Pb/^{204}Pb = 16.9373$ ,  $^{207}Pb/^{204}Pb = 15.4925$ , and  $^{208}Pb/^{204}Pb = 36.7054$ . The range of EPR (10-23°S) data (excluding sample MW 103-4 from Garrett FZ) is shown for comparison.

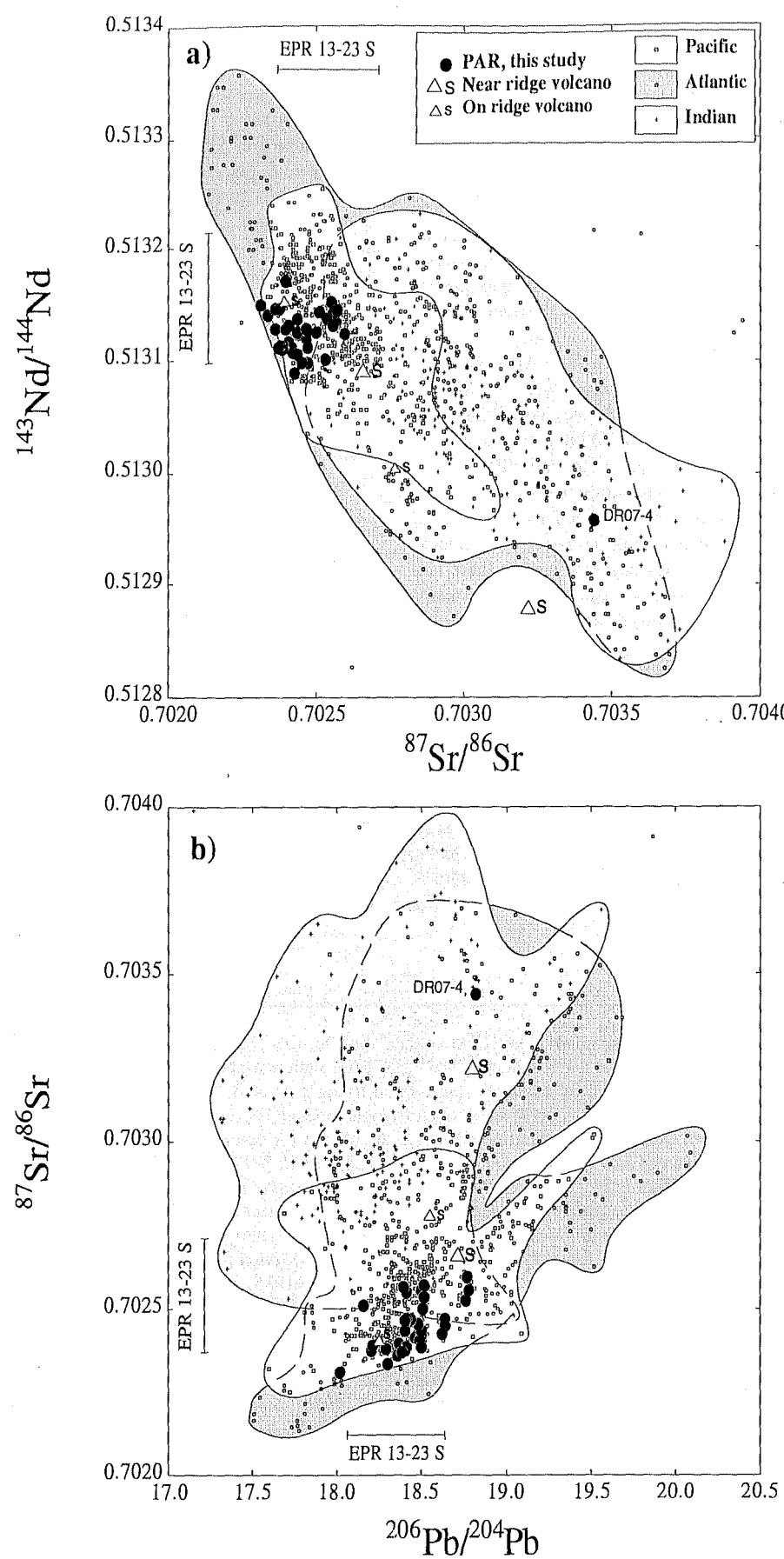
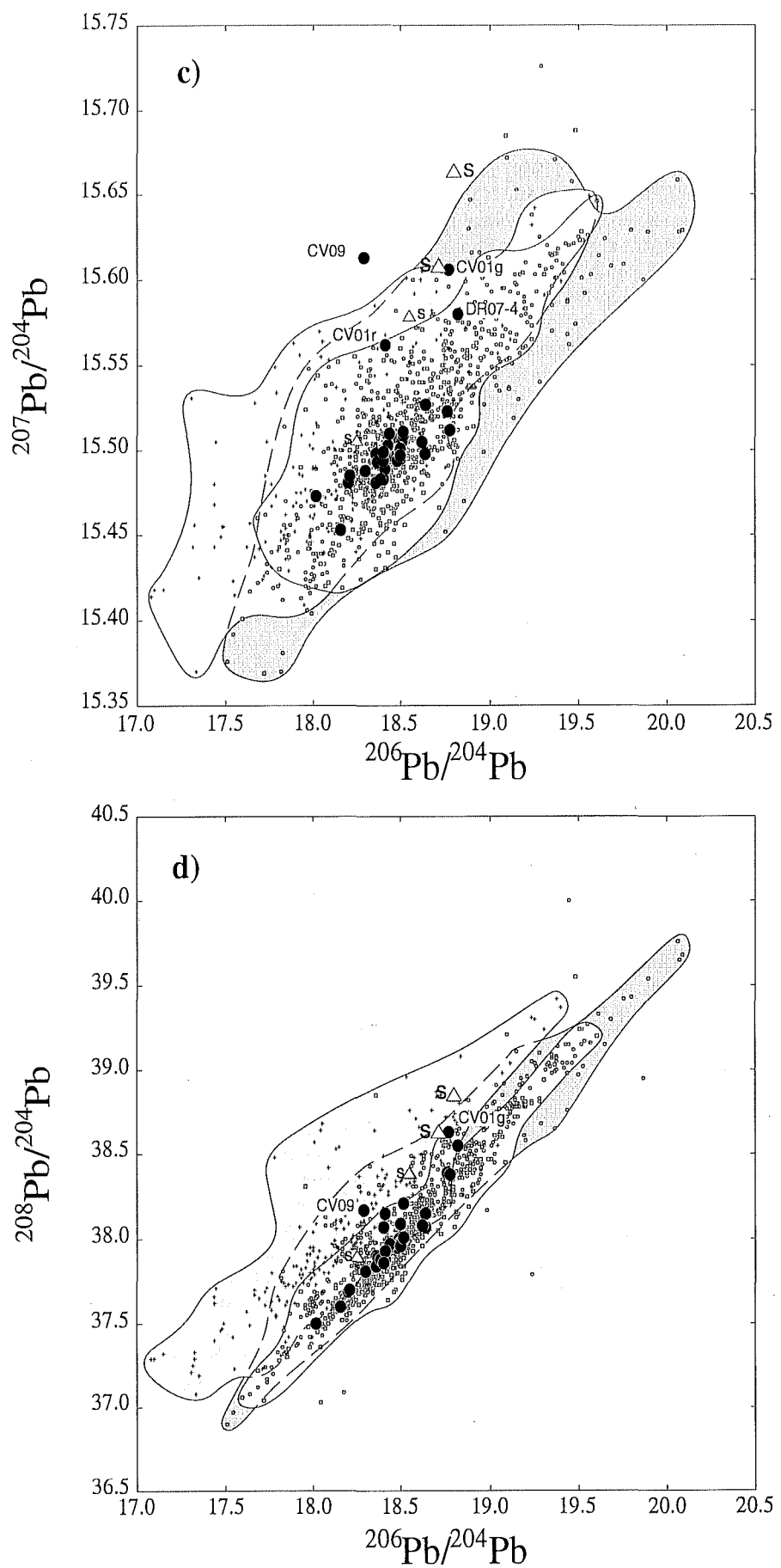


Figure 2.

**Figure 2.** (continued)

variations (see Figures 2a and 2b). The new compilation of MORB from the three oceans presented here emphasizes the great homogeneity of the mantle beneath the PAR.

Samples from the two seamounts (CV07 on-ridge and DR04 off-axis) display larger Sr, Nd, and Pb isotope ranges compared to normal ridge samples. Such an observation was first made by Zindler *et al.* [1984] and Castillo and Batiza [1989] for young seamounts in the vicinity of the EPR and the MAR. If CV07-r has globally similar isotopic signature compared to normal ridge samples, CV07-g, DR04-g, and DR04-2 display higher Sr and Pb and lower Nd isotopic ratios. The isotopic compositions of the two seamounts define linear trends in Sr-Nd and Pb-Pb plots. Samples CV01-r and CV01-g seem to belong to this correlation in both Pb-Pb plots (Figures 2c and 2d). The granodiorite DR07-4 displays Sr, Nd, and Pb isotopic values which cannot be included in on-axis sample systematics nor in the seamount systematics. It displays the highest Sr isotopic ratio found in the study area (0.703442). It will not be shown in the following along-axis plots. Sample CV09 has anomalous  $^{207}\text{Pb}/^{204}\text{Pb}$  and  $^{208}\text{Pb}/^{204}\text{Pb}$ , but  $^{206}\text{Pb}/^{204}\text{Pb}$  is in the range of other ridge samples.

The correlations between isotopic and trace element ratios are generally poor (not shown), due to the small variations of isotopic ratios. This is a characteristic of spreading ridges far from hotspot influence [Mahoney *et al.*, 1994].

#### 4.3. Along-Ridge Geochemical Variations

For convenience, the studied ridge length can be divided into seven segments, each one being between 180 and 300 km in length and being delimited by major ridge offsets (except the segment 2/segment 3 boundary at the tip of the 167W PR). Note that within the transitional domain the ridge is highly segmented. Thus the so-called segments 3 and 4 include Heitzler and Le Renard FZ, respectively.

Within the Pacific range of isotopic values (Figures 2a and 2b), 56–66°S PAR samples display a narrow range. Focusing on this narrow range, the data are scattered when plotted along the ridge axis according to the distance to the pole of rotation of the Pacific plate (Figure 3). This contrasts with the smooth and regular patterns displayed by isotopic ratios (with a similar range of variation) [Mahoney *et al.*, 1994] or the overall increase of trace element ratios along the EPR from 23°S to 10°S [Sinton *et al.*, 1991].

However, for most ridge segments,  $(\text{Nb}/\text{Zr})_N$  displays a systematic NE-SW decrease. This behavior is clearly observed along segments 3, 4, 6, and 7. Along segment 5, the highest  $(\text{Nb}/\text{Zr})_N$  values are found at both ends of the segment, possibly in relation with the fact that the SW end of segment 5 corresponds to the tip of the V, or is close to Le Petit Prince seamount. The maximum  $(\text{Nb}/\text{Zr})_N$  within each segment is nearly constant for the northern area and decreases from the tip of the V toward the south (dashed line in Figure 3).  $^{87}\text{Sr}/^{86}\text{Sr}$  values found at each NE end of a segment display a decreasing trend from Urdintsev FZ to the tip of the 167W PR. The  $(\text{Nb}/\text{Zr})_N$  variation, denoted  $\Delta(\text{Nb}/\text{Zr})_N$ , is defined as the difference between the highest and the lowest  $(\text{Nb}/\text{Zr})_N$  values for each segment. A clear southward decrease of  $\Delta(\text{Nb}/\text{Zr})_N$  is illustrated in Figure 4.

#### 5. Thermal Structure Beneath the PAR

Worldwide variations of ridge morphology have been ascribed to variations of spreading rate and mantle temperature [Phipps Morgan *et al.*, 1987; Chen and Morgan, 1990a, b; Phipps

Morgan and Chen, 1993]. Along the 56–66°S PAR, the valley-dome transition is associated with an increase of spreading rate. In this section we test the relationship between ridge morphology and mantle temperature. There are several methods to estimate the thermal structure of the mantle beneath a mid-ocean ridge. Variations in the mantle temperature can be inferred from gravity-derived crustal thickness, seismic velocities, or partial melting model studies. Here, we use our major element data set and two different petrological melting models: Klein and Langmuir, [1987, 1989] and Niu and Batiza, [1991] hereinafter referred to as KL87 and NB91, respectively.

#### 5.1. KL87 and NB91 Melting Models

Both melting models assume a homogeneous mantle source with respect to major elements. Such an assumption is discussed at length by Langmuir *et al.*, [1992] and Hofmann, [1988], who claimed that far from hotspots the mantle source is likely to be quite homogeneous for moderately incompatible and compatible elements. As shown in section 4 our PAR study area satisfies this condition quite well. Both models use 8% MgO normalized data in order to remove effects due to fractional crystallization during magma ascent. The KL87 model is based on theoretical determination of melt parameters using  $(\text{Na}_2\text{O})_{8.0}$  variations in basalts. Conversely, the NB91 model is based on experimental data from which they developed empirical relationships to quantify melting conditions using  $(\text{Na}_2\text{O})_{8.0}$ ,  $(\text{CaO})_{8.0}/(\text{Al}_2\text{O}_3)_{8.0}$  (for extent of melting) and  $(\text{FeO})_{8.0}/(\text{SiO}_2)_{8.0}$  (for melting depth) (Figure 5). Because of questions concerning the homogeneity of the mantle with respect to Na, a modified version of the NB91 model has been proposed [Niu, 1992], where the extent of melting is inferred only from  $(\text{CaO})_{8.0}/(\text{Al}_2\text{O}_3)_{8.0}$ . However, in this study, because we are far from any hotspot influence, we use the NB91 algorithm. It is worth noting that the KL87 model uses only one moderately incompatible element, whereas the NB91 model uses several compatible elements.

The first step in each model is to normalize the major elements to 8% MgO (here we assume that the correlation between major element oxides and MgO is due to fractional crystallization). Only microprobe measurements (MP) on hand-picked pieces of glass are used. The equations of the best linear regression lines (giving the slopes needed in the calculations) are given in the Figure 6 caption. The range of MgO values (6.2 to 8.8 wt %) suggests that variable fractional crystallization is important, whereas the small scatter for a given MgO content indicates little variation in parental magma composition itself being the result of small variations in source composition and/or melting extent. In turn, we note the following:

1. the resulting  $(\text{Na}_2\text{O})_{8.0}$  versus  $(\text{FeO})_{8.0}$  plot displays a negative correlation, termed “global trend” by Klein and Langmuir [1987, 1989] (Figure 5a). This plot shows that (1) samples located south of Saint Exupéry FZ (full spreading rate < 65 mm/yr,  $n = 12$ ) display a well-defined ( $r = 0.82$ ) correlation, slightly steeper than the one, poorly defined ( $r = 0.35$ ) by samples north of Saint Exupéry FZ (full spreading rate > 65 mm/yr,  $n = 24$ ), (2) these two slopes are smaller than the slope of the global trend defined for normal ridges Langmuir *et al.* [1992]. The existence of a global negative correlation between  $(\text{Na}_2\text{O})_{8.0}$  and  $(\text{FeO})_{8.0}$  has been ascribed to variations of mantle temperature [Klein and Langmuir, 1987], whereas their slopes are discussed in terms of style of mantle upwelling (active versus passive) [Niu and Batiza, 1993] or mantle heterogeneity (see discussion in section 7).

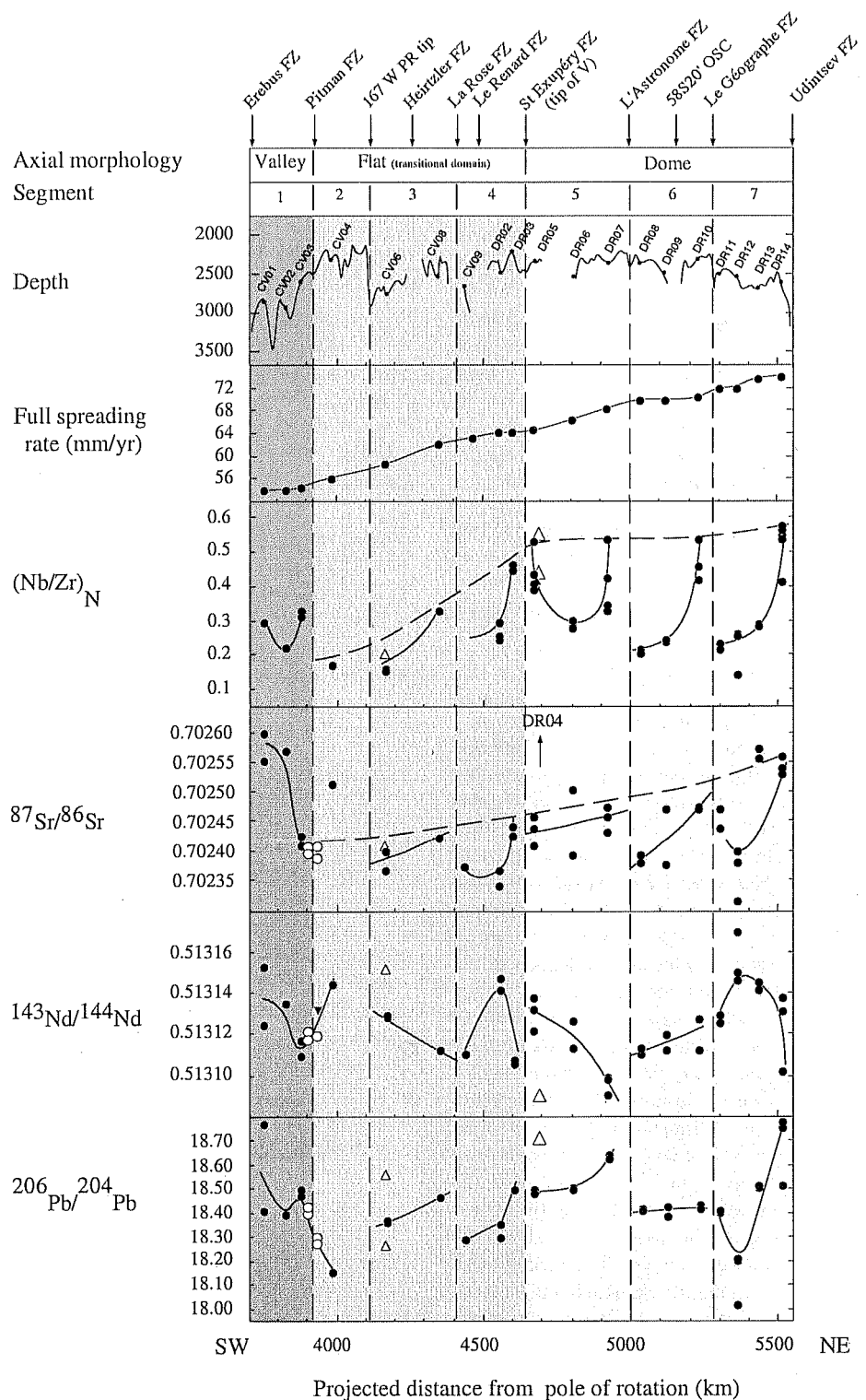


**Figure 3.** Along-ridge geochemical variations. Distances are in km from the Pacific plate pole of rotation ( $101^{\circ}\text{E}$ ,  $64.3^{\circ}\text{S}$ ). Boundaries of segments are indicated by dashed lines (see text). The three domains of different ridge morphological signatures (valley, flat, dome) are shown with different shades of gray. Spreading rate is from Sahabi et al. [1996]. Circles are for ridge samples (open circles are from Ferguson and Klein [1993]; solid circles are from this study). Open triangles are for seamount samples (this study). Normalizing values used to calculate  $(\text{Nb}/\text{Zr})_{\text{N}}$  are 0.465 for Nb and 5.13 for Zr.

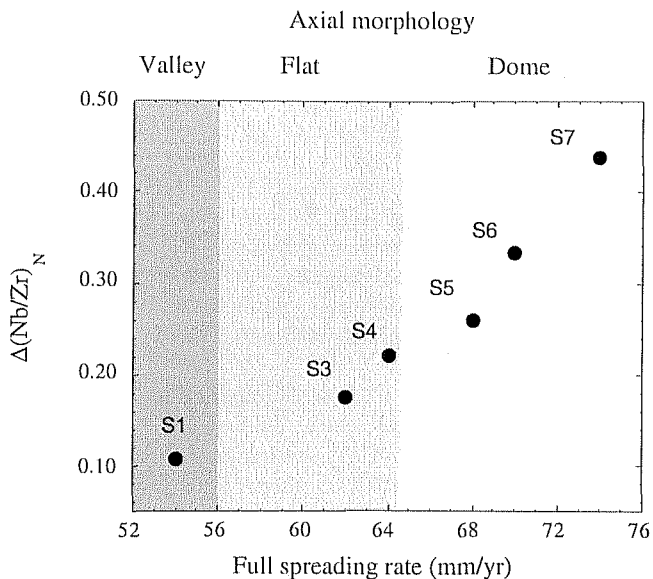


**Figure 4.** The  $(\text{Nb}/\text{Zr})_N$  variability versus spreading rate and axial morphology. The different shaded areas indicate, as in Figure 3, the three domains with different axial morphologies.  $\Delta(\text{Nb}/\text{Zr})_N = (\text{segment higher } (\text{Nb}/\text{Zr})_N \text{ value minus segment lower } (\text{Nb}/\text{Zr})_N \text{ value})$ .

2. the  $(\text{Na}_2\text{O})_{8.0}$  versus ridge depth plot (Figure 5b) displays a negative correlation, inverse to the one predicted by Klein and Langmuir [1987], suggesting that the lowest extents of melting occur at the shallowest depths. The slope of the correlation is very similar between the two selected areas, although better defined ( $r = 0.87$ ) for southern samples. This observation could suggest that the mantle potential temperature, i.e., the temperature at which the mantle intersects the solidus, does not control the PAR bathymetry.

The melting parameters resulting from the application of the two models to the PAR samples are shown in Figure 6 (see caption for details). Because NB91 use a higher value of  $dF/dP$  compared to KL87 (2-2.5%/kbar instead of 1.2%/kbar), their computed values of  $F$  are systematically higher. Our discussion and conclusions in sections 7 and 8 do not depend strongly on whether the extent of melting  $F$  inferred from NB91 represents the mean or maximum extent of melting [see Niu and Batiza, 1994; Niu et al., 1996]. However, in order to preserve the coherence of results between the two models we use (in figures and text) the mean extent of melting according to NB91 and the maximum extent of melting according to KL87. Although these models are based on different major elements and sets of assumptions, the relative patterns are similar. This reinforces our belief that the petrologically inferred thermal structure of the PAR mantle is rather robust. Nevertheless, we recognize that both models assume a perfectly homogenous mantle with respect to major elements, and thus both of them could be erroneous in the same way.

## 5.2. Results of the Models

Both models reveal a low extent of melting  $F$ , a low initial depth  $Z_0$ , and temperature of melting  $T_0$  in the middle of the study area, which corresponds to the tip of the V (Saint Exupéry FZ).  $F$ ,  $Z_0$ ,  $T_0$ , and crustal thickness  $Dc$  depend on the melting model but typically decrease by 2%, 10 km, 40°, and 2.5 km,

respectively, toward the V tip minima. The ranges of calculated melt parameters shown in Figure 6 are (1) similar to the ones deduced from 6-30°S EPR samples using the NB91 model [Bach et al., 1994], (2) smaller than those deduced from 5°N-7°S MAR samples using KL87 model [Schilling et al., 1995]. For the 56-66°S PAR the largest difference between the two models concerns the range of initial temperatures of melting (51° for KL87 versus 100° for NB91). This is due to the higher  $dF/dP$  value used by NB91. The NB91 model may be more sensitive than the KL87 model because it uses several elements (five against only one for the KL87 model). In the rest of the paper we use the NB91 model to discuss short-wavelength trends.

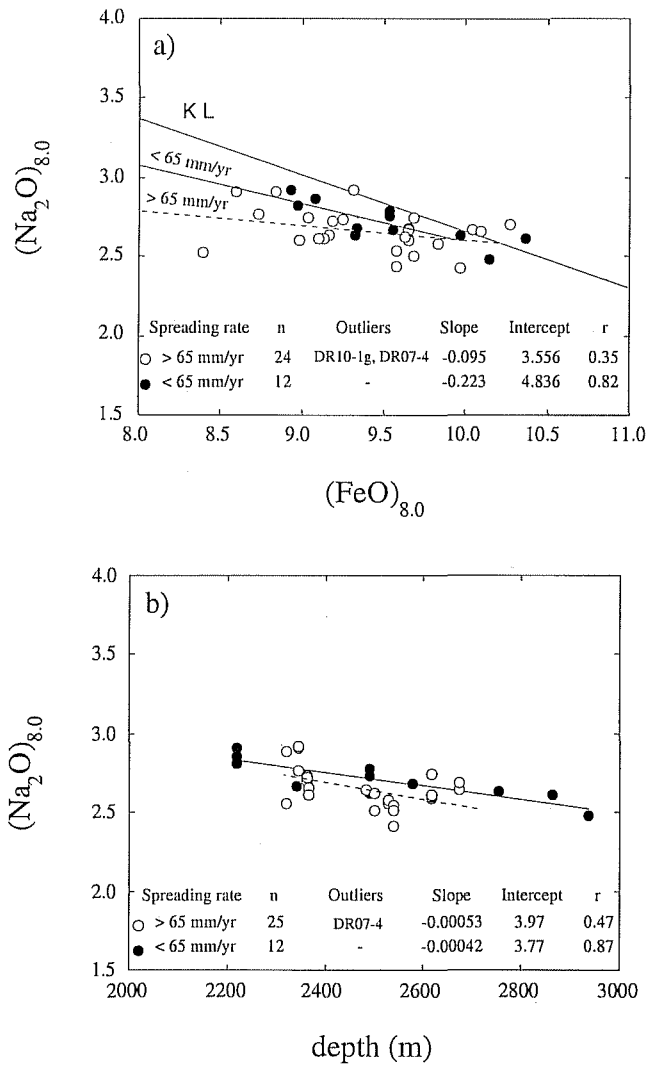


**Figure 5.** (a)  $(\text{Na}_2\text{O})_{8.0}$  versus  $(\text{FeO})_{8.0}$  plot for basalts for which MP data are available. The methodology used to calculate the fractionation corrected oxides is given in the Figure 6 caption. Global vector from normal ridges [Langmuir et al., 1992] (named KL) has for equation  $(\text{Na}_2\text{O})_{8.0} = -0.36 (\text{FeO})_{8.0} + 6.26$ . Solid symbols are for samples located south of Saint Exupéry FZ (full spreading rate < 65 mm/yr); open symbols are for samples located north of Saint Exupéry FZ (full spreading rate > 65 mm/yr). Slopes, intercepts, outliers; and coefficients of correlation of linear regression lines are indicated. (b)  $(\text{Na}_2\text{O})_{8.0}$  versus depth plot for basalts for which MP data are available. Symbols are as in Figure 5a. Slopes, intercepts, outliers and coefficients of correlation of linear regression lines are indicated.

In the northern part of our study area, characterized by a dome-like morphology, there is a systematic variation of calculated melt parameters in the vicinity of transform faults (Figure 7). This systematic behavior is real even when taking into account the error on  $F$  (which is less than the local variability) estimated from analytical error propagation (see Figure 7 caption). The low  $F$ ,  $Z_0$ , and  $T_0$  observed near Saint Exupéry FZ can be interpreted as indicating an edge effect similar to the "transform fault effect" (TFE) described by *Langmuir and Bender* [1984], i.e., cooling toward the surface is more efficient near the FZ than in the middle of segments, resulting in lower extent of melting (see section 7.2). For Le Géographe and L'Astronome FZs, the edge effect is present but is asymmetric in particular with respect to  $F$ : values found in the NE side of transform faults are higher than those found in the SW side. The edge effect is more symmetric with respect to  $T_0$ . Typically, from the NB91 melting model, transform faults decrease  $F$ ,  $Z_0$ , and  $T_0$  from 1%, 8 km, and 30°C (south of L'Astronome FZ) to 2%, > 20 km, and 80°C (south of Le Géographe FZ). In the southern domain (characterized by a valley-like morphology), Pitman FZ does not seem to produce any edge effect.

To summarize, melt parameter behavior in the northern part of our study area can be explained by (1) a slight increase of mantle temperature (~40°C) from SW to NE, (2) a superimposed TFE (up to 80°C according to the NB91 model south of Le Géographe FZ), and (3) an unknown mantle process creating asymmetric TFE. This latter can be a process which reduces or prevents edge effect in the north side of L'Astronome and Le Géographe FZ and/or enhances edge effect in the south side of fracture zones.

### 5.3. Relation With Trace Element and Isotopic Ratios

When plotted against the extent of melting (inferred from the NB91 model), trace element ratios display decreasing linear trends from  $F = 15.7$  to  $F \sim 18\%$  (Figure 8). For  $F$  above ~18%, trace element ratios remain nearly constant, likely being close to the source value. Exceptions are samples from dredge 14 and sample CV07-g which display both high extents of melting and high trace element ratios (typically,  $F = 18.3\%$  and  $(La/Sm)_N = 0.8$ ). Excluding these points, the resulting best fitting curves are exponential with a coefficient of correlation higher than 0.8. In contrast, there is not significant correlation between isotopic ratios and the extent of melting. These results contrast with those of *Niu et al.* [1996] on the 18–19°S EPR. There the extent of melting correlates both with trace element and isotopic ratios.

## 6. Long-Wavelength Trends

Compiling the results of this study with those recently published by *Castillo et al.* [1998] gives a continuous view of mantle characteristics from south of Pitman FZ to Vacquier FZ (Figure 1a). Sr, Nd, Pb isotopes,  $(La/Sm)_N$ , mantle-calculated temperature, and relative seismic velocities [*Roult et al.*, 1994] are shown in Figure 9. The most remarkable feature is the low variability of the three isotope ratios south of Uditsev FZ compared to the northern segments. The southwestward decrease of  $^{87}\text{Sr}/^{86}\text{Sr}$  appears to originate from the intersection of the Hollister Ridge with the PAR at 55°S. In contrast, the low  $^{143}\text{Nd}/^{144}\text{Nd}$  signature of Hollister Ridge does not seem to influence the PAR south of Uditsev FZ, where  $^{143}\text{Nd}/^{144}\text{Nd}$  remains nearly constant. Consequently, the southwestward increasing gradient of  $^{143}\text{Nd}/^{144}\text{Nd}$  suggested by *Castillo et al.*, [1998] south of Vacquier FZ clearly ends at Uditsev FZ.

$(La/Sm)_N$  seems to decrease slightly southwestward from Vacquier FZ ( $(La/Sm)_N \approx 0.8$ ) to south Pitman FZ ( $(La/Sm)_N \approx 0.45$ ). Mantle temperature inferred from the KL87 melting model shows three coherent trends with similar amplitudes (30–40°C) and scales (~1000 km): going south from Vacquier FZ an increasing trend occurs up to 57.2°S (dredge 12 location between Uditsev and Le Géographe FZ), then a decreasing trend occurs down to Saint Exupéry FZ (the tip of the V) and finally an increasing trend occurs up to south Pitman FZ. The resulting global variation of mantle temperature is a slight increase of ~30° toward the southwest (1340°C near Vacquier FZ to 1370°C south of Pitman FZ). To summarize, mantle temperature seems to increase continuously towards the southwest except inside the V where a reverse trend is observed. High-resolution (500 km) seismic velocities are shown for three periods ( $T = 76$  s,  $T = 100$  s and  $T = 200$  s corresponding respectively to depths of penetration of ~122 km, 160 km, and 320 km [*Roult et al.*, 1994]). From Vacquier FZ to 57.2°S the three velocities decrease coherently and also agree with the increasing mantle temperature inferred from melt parameters. South of 57.2°S, there is no more coherency between seismic velocities, and none of them behave similarly to melt parameters.

## 7. Discussion

### 7.1. Regional Homogeneity of the Mantle South of Uditsev FZ

From south Pitman to Uditsev FZ the 1800-km-long ridge section samples a depleted mantle. As the spreading rate increases from SW to NE, so does the geochemical variability (Figures 3 and 4). If mixing is a dominant process at fast spreading ridges [*Allègre et al.*, 1984; *Batiza*, 1984], a decrease in geochemical variability is expected toward the NE. This is not supported by the observations reported earlier; therefore there is no straightforward relationship between spreading rate and mixing. Thorough mixing could result from high melt flux regardless of spreading rate, but high melt flux would be expressed by an axial high such as observed in the northern part of the area where geochemical variability is the highest. Hence another process must be invoked (see section 7.4.1).

The slight increase of  $^{87}\text{Sr}/^{86}\text{Sr}$  or  $(La/Sm)_N$  toward the northeast could suggest a small influence of an enriched mantle source located north of Uditsev FZ. Because of their vicinity and well-marked enriched signatures, Hollister Ridge and Louisville hotspot [*Vlastelic et al.*, 1998; *Cheng et al.*, 1987] are preferred candidates. However, neither  $^{143}\text{Nd}/^{144}\text{Nd}$  nor  $^{206}\text{Pb}/^{204}\text{Pb}$  supports this hypothesis, indicating that if the influence exists, it is very weak. According to trace element ratios versus extent of melting plots (Figure 8), only samples from dredge 14, just south of Uditsev FZ, indicate the presence of significantly more enriched mantle. Uditsev FZ appears as a limit between two regions, one to the north with large isotopic variation and one to the south where the isotopic variations are much more subdued.

It has been previously noted that PAR basalts display low  $^{143}\text{Nd}/^{144}\text{Nd}$  and high  $^{206}\text{Pb}/^{204}\text{Pb}$  for a given  $^{87}\text{Sr}/^{86}\text{Sr}$  compared to northern EPR basalts [*Vlastelic et al.*, 1999]. These characteristics are similar to those observed along the 30–35°S EPR [*Macdougall and Lugmair*, 1986; *White et al.*, 1987; *Bach et al.*, 1994], where it has been suggested that small amounts of HIMU end component (high  $^{206}\text{Pb}/^{204}\text{Pb}$  and low  $^{87}\text{Sr}/^{86}\text{Sr}$ ) might

be influencing the source of MORB [Mahoney *et al.*, 1994]. The vicinity of the Foundation Chain (EPR 38°S) with clear HIMU affinity [Hémond and Devey, 1996] supports this hypothesis. Similar explanation could also hold for the PAR if we consider that HIMU signature has been reported from a large area extending between Tasmania, New Zealand, and Antarctica [Lanyon *et al.*, 1993]. The closest sample (CV01) to the Balleny hotspot (66.58°S, 162.93°E) which presents a HIMU signature [Green, 1992; Lanyon *et al.*, 1993] is located at a distance of ~1070 km (see Figure 1) at the southwestern end of the studied ridge section. However, according to what is actually known on ridge-hotspot interactions, it is unlikely that the higher Pb and Sr isotopic ratios measured on sample CV01-g reflect an influence of the hotspot source. This, however, can be questioned by the recent work of Niu *et al.* [1999], who emphasize the remote influence of a plume (Hawaii) on a spreading ridge (EPR). Nevertheless, a general HIMU affinity of the southern Pacific upper mantle is suggested by the data from the South East Indian Ridge (SEIR) east of the Australian-Antarctic Discordance (AAD) [Klein *et al.*, 1988; Pyle *et al.*, 1992], the EPR south of 25°S [White *et al.*, 1987; Bach *et al.*, 1994], and the PAR. The HIMU affinity could be revealed by a larger variability (expressed by  $\sigma/m$ , see Table 2) in Pb isotopes than in Sr and Nd, which is indeed what is observed for southern Pacific samples (Table 2).

The higher variability of Pb compared to Sr and Nd is also present for northern Pacific samples. It suggests another type of interpretation which would take into account the different half-lives of the parent nuclides. The decay constants decrease in the same order as the observed variability of the corresponding isotopic ratios ( $\lambda^{147}\text{Sm} < \lambda^{87}\text{Rb} < \lambda^{238}\text{U}$ ). As a consequence, any fractionation event occurring in the mantle will be more rapidly

recorded by  $^{206}\text{Pb}/^{204}\text{Pb}$  than by  $^{143}\text{Nd}/^{144}\text{Nd}$ , creating with time more variability in Pb than in Sr and Nd isotopic ratios. Therefore it can be predicted that the relative high Pb isotopic variability can be generalized to the global spreading system. Indeed, a similar observation has recently been made along the MAR, together with a discussion on the age of the mantle fractionation event [Dosso *et al.*, 1999].

## 7.2. Local Variability: Small-Scale Heterogeneity or Melting Process?

From the description in section 7.1 of the data we have seen that PAR (56–66°S) geochemical variability occurs essentially at the segment scale. The question now is whether this variability reflects a property of the underlying mantle or not. The relation between geochemical variations and segmentation suggests that part of the geochemical variability could result from processes occurring in the vicinity of transform faults (Figure 3). A decrease in melting extent resulting from cold edge effect near the transform was proposed by Langmuir and Bender [1984], although this interpretation was later reevaluated by Bender and Langmuir [1985], invoking different stages of tectonic and chemical cycles.

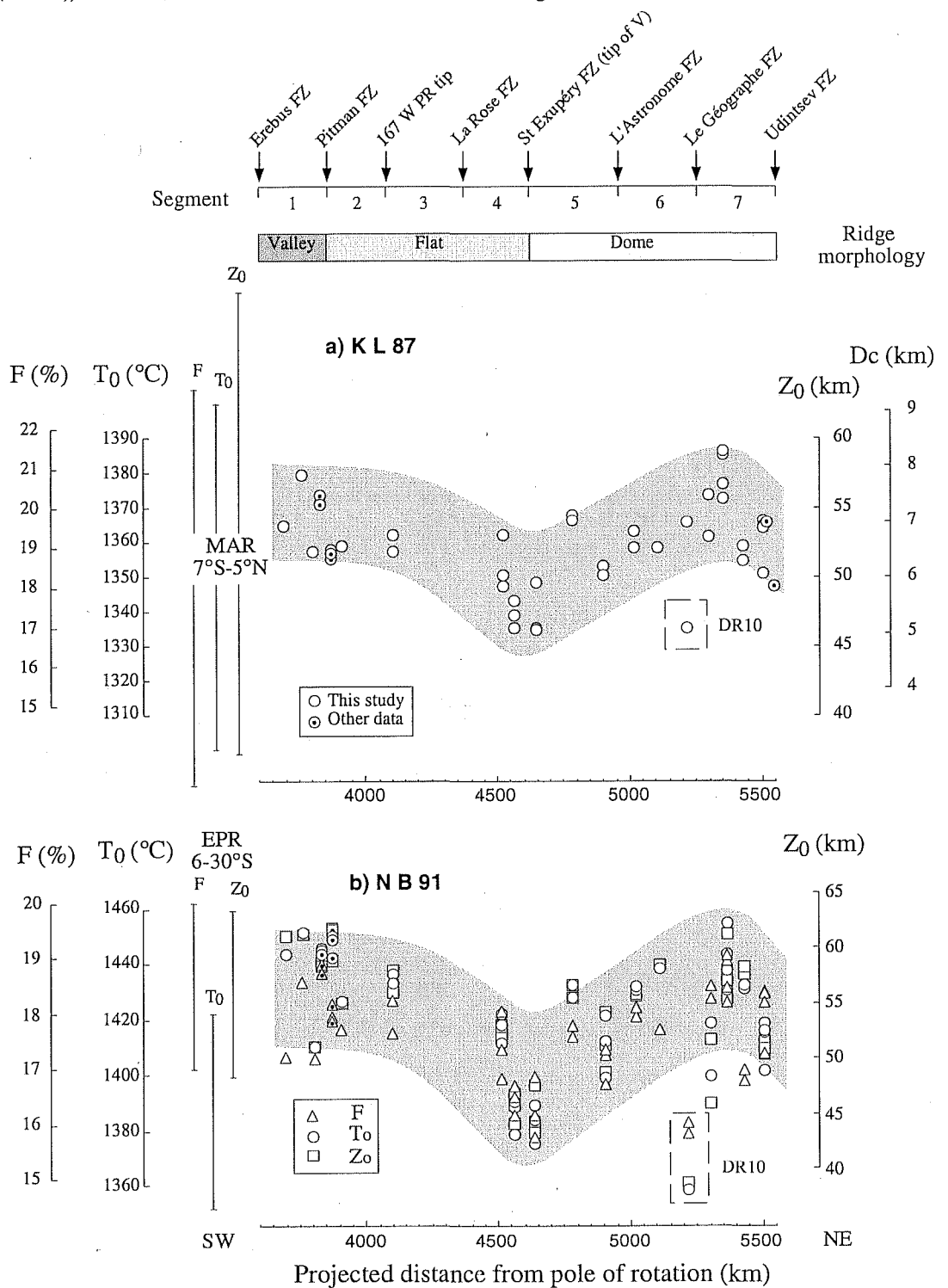
We will first assume a homogeneous depleted mantle source with respect to Nb and Zr along the PAR ( $\text{Nb}_0 = 0.28 \text{ ppm}$ ,  $\text{Zr}_0 = 8.4 \text{ ppm}$  [from Johnson *et al.*, 1990]), crystal-liquid distribution coefficients ( $D_0 \text{ Nb} = 0.0016$ ;  $D_0 \text{ Zr} = 0.018$  for spinel-garnet transition domain [from Gurenko and Chaussidon, 1995]) and a simple batch model [Shaw, 1970] (for which the results closely resemble those from mixing of melts throughout the melting regime [see Langmuir *et al.*, 1992]). A decrease in the mean melting extent of 1% (from 10 to 9%) increases  $(\text{Nb/Zr})_N$  from

**Figure 6.** (opposite). PAR thermal structure inferred from the KL87 and NB91 melting models. Data are plotted according to their projected distance to pole of rotation (see Figure 3). Open symbols are from this study; circled dots are from Castillo *et al.* [1998] and Ferguson and Klein [1993]. The shaded area indicates the large-scale trend of melt parameters. (a) The KL87 model. Maximum extent of melting  $F$ , corresponding initial depth  $Z_0$  and temperature  $T_0$  at which decompression melting begins, and crustal thickness  $D_c$  are derived from the KL87 petrologic decompression melting model, using the  $\text{Na}_2\text{O}$  content at  $\text{MgO} = 8\%$  ( $(\text{Na}_2\text{O})_{8.0}$ ) as a filter of low-pressure fractional crystallization. Both KL87 and NB91 models use 8% MgO normalized data. For the oxide  $X$  and sample  $i$ , the 8% MgO normalized value is expressed as  $(X_i) = S [(8 - (\text{MgO})) + (X_i)]$  where  $S$  is the slope of the regression line in the  $X$  against  $\text{MgO}$  plot and  $(\text{MgO})_i$  is the  $\text{MgO}$  content of the sample  $i$ . The equations of the best linear fit lines which slopes are used to correct for low pressure fractionation in the KL87 and NB91 melting models are  $(\text{Na}_2\text{O}) = 4.8774 - 0.27459(\text{MgO})$ ,  $R = 0.80$ ;  $(\text{FeO}) = 19.722 - 1.2854(\text{MgO})$ ,  $R = 0.89$ ;  $(\text{CaO}) = 5.4172 + 0.78863(\text{MgO})$ ,  $R = 0.89$ ;  $(\text{Al}_2\text{O}_3) = 8.2461 + 0.84151(\text{MgO})$ ,  $R = 0.92$ ;  $(\text{TiO}_2) = 4.9611 - 0.4526(\text{MgO})$ ,  $R = 0.89$ ;  $(\text{SiO}_2) = 51.299 - 0.071952(\text{MgO})$ ,  $R = 0.14$ .  $F$  is obtained from equation (7) of Plank and Langmuir [1992]:  $\langle C_L \rangle = (2C_S/F^2)\{F + (D/(D+1))[(1 - F)^{(D+1)/D} - 1]\}$  where  $\langle C_L \rangle$  is mean concentration in the accumulated melt,  $C_S$  is  $\text{Na}_2\text{O}$  concentration in the mantle source, taken as being equal to 0.3 wt % [Klein and Langmuir, 1987], and  $D$  is the bulk initial crystal/melt partition coefficient for  $\text{Na}_2\text{O}$  assumed to be equal to 0.03. Because equation (7) of Plank and Langmuir [1992] can not be inverted, the maximum melt fraction  $F$  in a unit column at the ridge axis is obtained by iteration for each sample. Assuming a constant value of  $(dF/dP) = 1.2\%/\text{kbar}$ , the relationships used to calculate  $P_0$ ,  $P_f$  (initial and final depth of melting),  $T_0$ ,  $T_f$  (initial and final temperature of melting) and  $D_c$  (crustal thickness) are  $F = 0.012(P_0 - P_f)$ ;  $P_f = F^2/0.024$ ;  $T_0 = 1150 + 12P_0$ ;  $D_c = 0.006(P_0 - P_f)^2(10.2/\rho_c) = 162.14F^2P_0^{0.038}$  with  $P$  in kilobars,  $T$  in degrees Celsius,  $F$  as a fraction,  $\rho_c$  as the density of the crust assumed to be 2.62 g/cm<sup>3</sup>. A mantle density of 3.3 g/cm<sup>3</sup> is assumed to convert  $P$  into  $Z$ . For comparison, MAR 5°N–7°S ranges of  $F$ ,  $Z_0$ ,  $T_0$  are shown (data from Schilling *et al.* [1995]). (b) the NB91 model.  $F$ ,  $Z_0$ ,  $Z_f$ ,  $T_0$ ,  $T_f$  (notations are the same as for figure 6a) are from Niu and Batiza [1991]. The equations used are:  $F = 19.202 - 5.175(\text{Na}_2\text{O})_{8.0} + 15.537[(\text{CaO})_{8.0}/(\text{Al}_2\text{O}_3)_{8.0}]$ ;  $P_0$  (kbar) =  $25.98 + 0.967F + 45.277/F - 5.186[(\text{SiO}_2)_{8.0}/(\text{FeO})_{8.0}]$ ;  $P_f$  (kbar) =  $(1.3613P_0 + 3.9103) + (-1.3458P_0 - 13.592)/F + (-0.03015P_0 - 0.2929)F$ ;  $T_0$  (°C) =  $(F - a - bP_0)/(c + dP_0)$ ;  $T_f$  (°C) =  $(F - a - bP_f)/(c + dP_f)$  with  $a = -117.149$  (kbar<sup>-1</sup>);  $b = -6.028$  (°C<sup>-1</sup>);  $c = 0.11679$ ;  $d = 3.02310^{-3}$  (kbar<sup>-1</sup> °C<sup>-1</sup>);  $a - b - c - d$  empirical coefficients are for the Tinaquillo Iherzolite [see Niu and Batiza, 1991]. A mantle density of 3.3 g/cm<sup>3</sup> is also assumed to convert  $P$  into  $Z$ . For comparison, 6–30°S EPR ranges of  $F$ ,  $P_0$ ,  $T_0$  are shown (data from [Bach *et al.*, 1994]).

0.421 to 0.427, and a decrease of 10% (from 15 to 5%) increases  $(\text{Nb/Zr})_N$  from 0.402 to 0.479. Both of these variations are much less than the observed  $(\text{Nb/Zr})_N$  variations along the PAR (0.15 to 0.58). This first suggests that an important part of  $(\text{Nb/Zr})_N$  variations reflects changes in source composition. It is, however, possible to account for PAR  $(\text{Nb/Zr})_N$  variations in the context of a homogeneous mantle if very low extents of melting of a highly depleted mantle source are considered. For example, with  $\text{Nb}_0 = 0.1 \text{ ppm}$  and  $\text{Zr}_0 = 7 \text{ ppm}$  as source concentrations, the range of  $(\text{Nb/Zr})_N$  observed along the PAR requires variation of the extent of melting from 0.5% ( $(\text{Nb/Zr})_N = 0.55$ ) to more than 10% ( $(\text{Nb/Zr})_N = 0.18$ ). However, can melt fractions as small as 0.5%

be extracted from the mantle? According to *McKenzie* [1985], a realistic value of the porosity within the melting column is 1%, also corresponding to a threshold value for melt separation of 0.85%. At this stage, we conclude that a mantle source nearly homogeneous with respect to trace elements cannot be excluded. Two observations support the idea that along the PAR south of Urditsev FZ, petrogenetic processes control the first-order trace element variations:

1. Evidence is given by dredge 10 samples, which display a large range of trace element concentrations with nearly constant isotopic ratios between the two analyzed samples of this dredge.



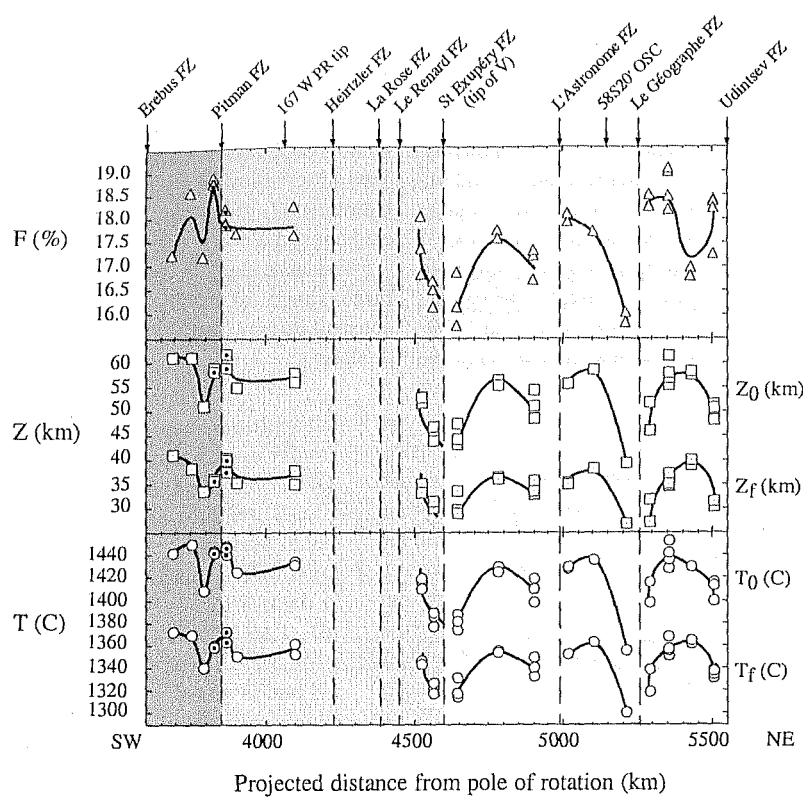


**Figure 7.** Behavior of melts parameters inferred from the NB91 model ( $F$ ,  $Z_0$ ,  $Z_f$ ,  $T_0$ ,  $T_f$ , notations are the same as in Figure 6) in the vicinity of transform faults. As in Figure 3, data are plotted according to their projected distance to pole of rotation. The different shaded areas indicate the three domains with different axial morphologies. Dots inside are from Ferguson and Klein [1993]. From the analytical error on major element concentrations (the relative error for each oxide is  $<0.5\%$ ), the precision on  $F$  is estimated to be better than  $0.1\%$  (absolute error).

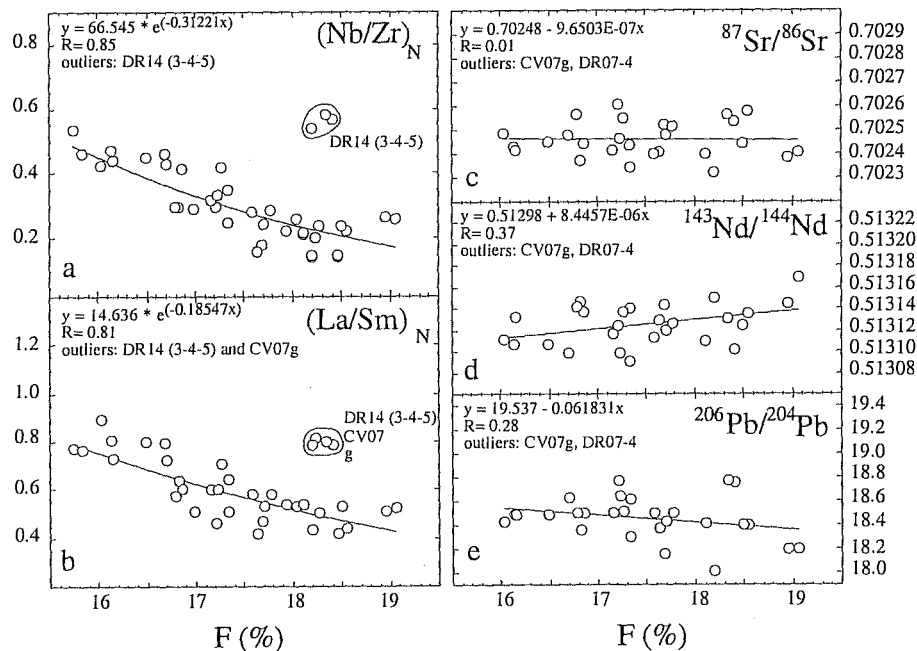


**Figure 8.** (a and b)  $(La/Sm)_N$  and  $(Nb/Zr)_N$  versus extent of melting inferred from the NB91 model. Best exponential fitting curves, outliers, equations, and coefficients of correlation are indicated. (c-e) Isotope ratios versus extent of melting inferred from the NB91 model. Best linear fitting curves, outliers, equations (figures 8a-8e) and coefficients of correlation are indicated. Only on-ridge samples are considered. Errors on all parameters are smaller than the symbol size.

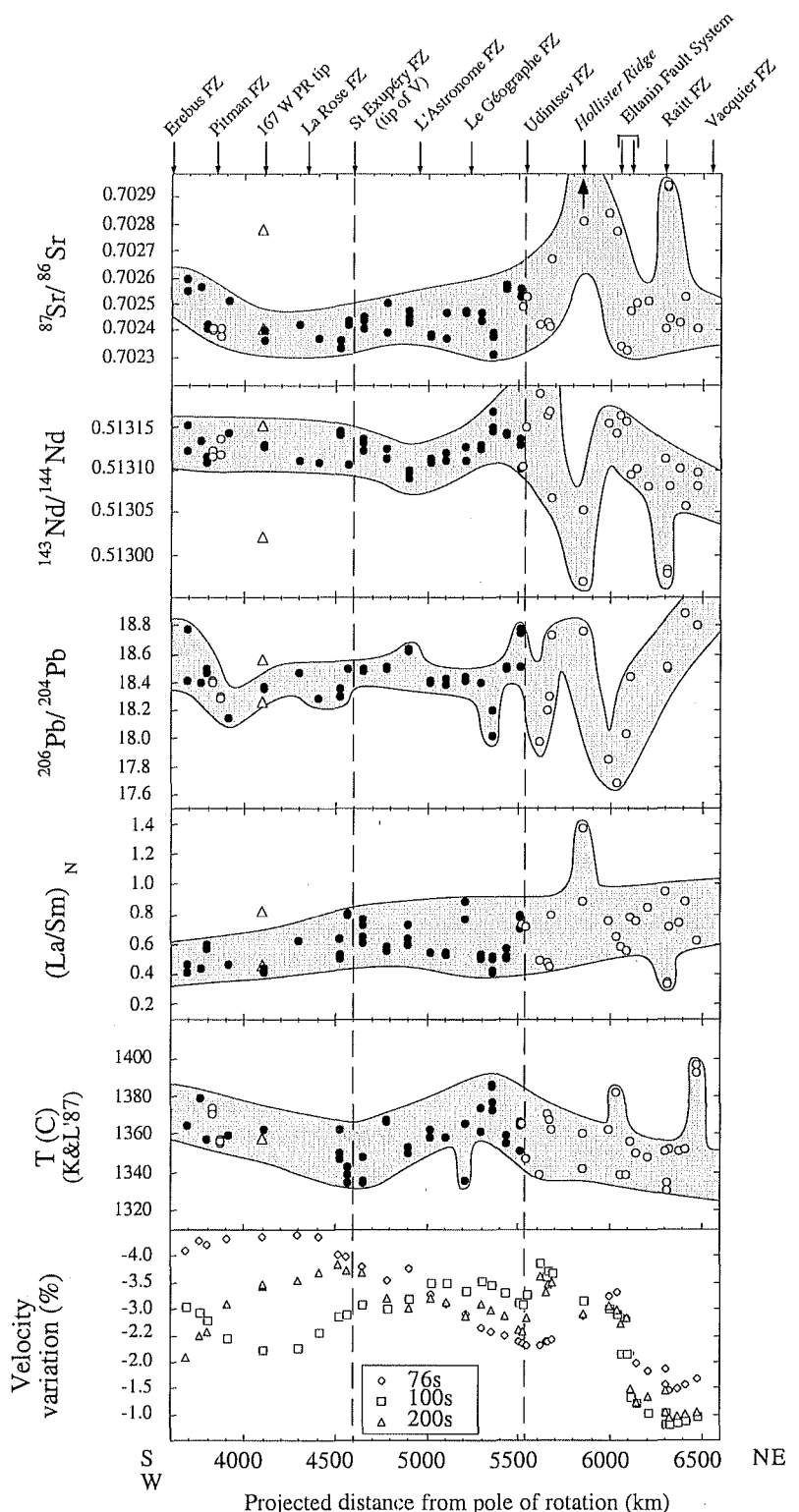


**Figure 9.** Compilation of data available on ridge basalts from south Pitman FZ to Vacquier FZ. Isotopic data,  $(\text{La}/\text{Sm})_N$ , and initial temperature of melting (inferred from the KL87 melting model according to the method described in Figure 6 caption) are from this study (solid circles and open triangles) and from Castillo et al. [1998] and Ferguson and Klein [1993] (open circles). The KL87 model is used because only  $(\text{Na}_2\text{O})_{8.0}$  is given by Castillo et al. [1998]. Seismic velocity data are from Roult et al. [1994]. The correlation length is 500 km. Velocity variations (%) correspond to the Swave velocity deviation from a reference velocity of  $3.98 \text{ km s}^{-1}$  ( $T = 76 \text{ s}$ ),  $4.06 \text{ km s}^{-1}$  ( $T = 100 \text{ s}$ ) and  $4.55 \text{ km s}^{-1}$  ( $T = 200 \text{ s}$ ). As in Figure 3, data are plotted according to their projected distance to pole of rotation.

2. Trace element ratios versus extent of melting display quite convincing correlations, whereas isotope ratios do not (see Figure 8). For a mean extent of melting (according to NB91) higher than 18%, trace element ratios measured in the erupted rocks would equal source composition with  $(\text{La}/\text{Sm})_{\text{N}} = 0.5 \pm 0.1$  and  $(\text{Nb}/\text{Zr})_{\text{N}} = 0.20 \pm 0.07$ . Samples from dredge 14 display both high trace element ratios and high extents of melting, suggesting the presence of a mantle source enriched in incompatible elements. Such heterogeneity at the dredge 14 location is not surprising, given the large variations of mantle composition occurring just north of Udintsev FZ.

This view, in which all the chemical variability results from variations in the extent of melting of a homogeneous mantle source, would be satisfactory if (1) the variations of melting extent inferred from major element models, typically 2%, agreed with those inferred from trace element modeling (typically 10 %) and (2) isotope ratios remained constant.

Reconciling major and trace element variations is a severe problem that has been discussed several times [Langmuir *et al.*, 1992; Devey *et al.*, 1994; Niu *et al.*, 1996]. Two main processes have been suggested: (1) sampling mantle heterogeneities [Langmuir and Bender, 1984; Sleep, 1984, 1988]; a mantle which is homogeneous with respect to major elements but heterogeneous with respect to trace elements is required, and (2) variation of the efficiency of extraction of the first melts from the deep regions of the mantle [Devey *et al.*, 1994]; no heterogeneous mantle source is required. Our data do not allow to favor one hypothesis over another.

The second problem (isotopic ratio variation) can be circumvented by assuming preferential melting of small mantle domains (smaller than the melting zone), more fertile and isotopically radiogenic [Langmuir and Bender, 1984]. Low extents of melting are expected to sample mainly enriched material, whereas higher extents of melting would average the properties of mantle components, resulting in a less enriched signature. However, the lack of correlation between isotopic ratios and the extent of melting (Figure 8) does not support this scenario, suggesting that the mantle is isotopically heterogeneous at a scale larger than the one of the melting zone.

### 7.3. Mantle Dynamics: Asthenospheric Flow?

Several morphologic and geochemical studies of the southern Pacific ridges have proposed that the Pacific upper mantle is flowing southwestward [Marks and Stock, 1994; Sahabi *et al.*, 1996; Castillo *et al.*, 1998]. In the frame of this geochemical study the flow hypothesis can be tested by tracking southward the mantle heterogeneity revealed north of Udintsev FZ. The fact that the geochemical gradients ( $^{143}\text{Nd}/^{144}\text{Nd}$ ,  $(\text{Na}_2\text{O})_{8.0}$ ,  $(\text{TiO}_2)_{8.0}$ ) identified by Castillo *et al.* [1998] north of Udintsev FZ do not extend farther south does not support the flow model. However, several observations could be related to the speculated flow: (1) the slight overall decrease of  $(\text{La}/\text{Sm})_{\text{N}}$  toward the southwest, (2) the presence of a relatively enriched mantle just south of Udintsev FZ (revealed by the conjunction of high extent of melting and elevated trace element ratios, see Figure 8a and 8b), (3) intrasegment asymmetric patterns  $((\text{Nb}/\text{Zr})_{\text{N}}, {^{87}\text{Sr}}/{^{86}\text{Sr}})$  identified in the northern part of our study area (Figure 3). If these three observations are compatible with the flow hypothesis, none of them provides any evidence for along ridge mantle material motion. In our view, asymmetric patterns are the most convincing indicators.

An asymmetric TFE is suggested by the behaviors of both  $(\text{Nb}/\text{Zr})_{\text{N}}$  and the extent of melting  $F$  in the vicinity of

L'Astronome and Le Géographe FZ (within the V). A quite consistent explanation of asymmetric TFE is given by Langmuir and Bender [1984] in the context of a propagating rift. Indeed, the propagating rift entering cold lithosphere is expected to show more important TFE than the dying rift retreating from the cold limb. This hypothesis should however be ruled out along the PAR because the V is characterized by a smooth seafloor without any evidence for dying or propagating rift. Vogt and Johnson [1975] suggested that the transform fault could block or at least impede along ridge mantle flow. The effect of a hot mantle flow at transform fault would be (1) to reduce or prevent edge effect at the FZ side which is exposed to the flow ("hot edge") and (2) to enhance edge effect at the FZ side which is sheltered from the flow ("cold edge"). Very low degrees of melt are expected where a cold edge occurs (SW side of FZ), and higher degrees of melt are expected at the hot edge (NE side of FZ). This hot mantle flow model could in first approximation account for the observed asymmetric TFE. Another possibility is that each segment is supplied by a diapiric upwelling, and the mantle flow sways the diapir closer to the NE side of the FZ, away from the SW side. Whatever the process occurring (TFE or diapir), the asymmetric patterns point out to a mantle flow.

### 7.4. Geochemistry and Physical Characteristics of the Ridge

**7.4.1. Geochemistry and segmentation.** Geochemical variations are closely linked to ridge segmentation, suggesting that transform faults may have an important control on the thermal structure of the shallow mantle. This is likely to be a general process along the global spreading system, but it could often be masked by the heterogeneity of the mantle source. The PAR between 56°S and 66°S, which appears, from the isotopic point of view, to sample a rather homogeneous mantle province, might be a privileged area to observe such process. According to NB91 algorithms, both initial and final depths of melting decrease near the FZ along the PAR (except Pitman FZ, Figure 7). However the cold edge effect drastically fades away in the first few tens of kilometer depth [Phipps Morgan and Forsyth, 1988], making it unlikely to have a significant influence on the base of the melting column. Supporting this idea, the modified equations of NB91 applied along the MAR (at 26°S, a region unaffected by hotspots) [Niu and Batiza, 1994] indicate a nearly constant initial depth of melting and much more variations in the final depths of melting. Identical conclusions were obtained by Shen and Forsyth [1995]. According to this view, far from any hotspot influence, a thin layer of mantle beneath the crust would display significant variations of temperature in response to the surface cold effects. Beneath this layer and far from hotspots, the along ridge variations of temperature could be very limited.

In the northern part of our study area, the melt parameters computed according to NB91 generally decrease in the vicinity of fracture zones, whereas they do not in the southern part (Figure 7). At the same time, trace element ratio variability (inferred from  $\Delta(\text{Nb}/\text{Zr})_{\text{N}}$ ) displays a well-marked southwestward decreasing trend (Figure 4). From these two observations and taking into account that trace element ratios are closely dependent on the extent of melting (Figure 8), it is suggested that the TFE magnitude decreases toward the southwest. According to Langmuir and Bender, [1984], the age of the truncating lithosphere should control the magnitude of the TFE. However, this effect cannot account for the observed variation of TFE magnitude on PAR because transform fault offsets do not display any along-ridge systematic variation (see Figure 1b). The

remaining candidates are spreading rate and ridge morphology. For a given offset it could be predicted that the higher the spreading rate, the lower the difference of temperature between the two adjoining lithospheres; therefore the lower is the TFE magnitude. Consequently, spreading rate is expected to produce an inverse trend of TFE magnitude compared to the one observed along the PAR. Finally, it is suggested that the cold edge is more effective in the axial dome context, resulting in an increase of the TFE magnitude along the valley-dome morphological transition.

**7.4.2. Axial morphology and mantle temperature.** One of the main goals of the Pacantarctic cruise was to see how the transition from dome-like to valley-like ridge axis morphology was recorded in basalt chemistry and derived mantle temperature. Along the South-East Indian Ridge (SEIR) between 88°E and 118°E, it has been shown that the dome-valley morphological transition occurs at constant spreading rate (74-76 mm/yr) and is associated with a lowering of mantle temperature (25-50°) [Shah and Sempéré, 1998]. There the agreement between temperature variations inferred from melting model and those inferred from gravity-derived crustal thickness suggests that this relationship does exist. Along the 56-66°S PAR, this transition is neither recorded by melt parameters nor by seismic velocities, indicating that the mantle temperature does not play an active role in controlling the axial morphology. Such an observation raises questions about the origin of the process which governs axial morphology: mantle temperature is suggested along the SEIR, whereas spreading rate is suggested along the PAR. Probably, none of these two factors alone controls directly ridge morphology. Instead, the rate of magma supply, which is itself likely to be controlled by both mantle temperature and spreading rate, could be the main contributing factor.

**7.4.3. Geochemistry and spreading rate.** The most convincing correlation between chemistry and spreading rate comes from trace element variability (deduced from  $\Delta(\text{Nb}/\text{Zr})_N$ ) which increases with increasing spreading rate. As mentioned above, this trend is likely to be controlled by variable TFE occurring in different ridge morphology contexts.

The relation between spreading rate and mantle temperature inferred from the chemical properties of MORB is debated. Some studies have concluded that the average temperature in the region of melting below mid-ocean ridges is independent of spreading rate [Langmuir et al., 1992; Niu and Batiza, 1993]. Others studies have predicted a relation between the spreading rate and the thermal structure of the mantle (extent of melting, crustal thickness) [Niu and Hekinian, 1997; Su et al., 1994; Bown and White, 1994]. This relation does not hold for the 56-66°S PAR, where melt parameters do not correlate with spreading rate.

Niu and Batiza [1993] proposed that the slope of  $(\text{Na}_2\text{O})_{8.0}$  versus  $(\text{FeO})_{8.0}$  plot is related to the spreading rate and corresponding style of upwelling. A negative correlation would occur at a fast spreading ridge (>60 mm/yr) and would indicate a passive upwelling in response to plate separation. A positive correlation would occur at a slow spreading ridge (<50 mm/yr) and would arise from processes occurring in buoyant diapirs. This interpretation holds along the PAR because with a full spreading rate range of 54-74 mm/yr, the PAR predicted slope is slightly negative (Figure 5a). However, it holds only partly because, as illustrated in Figure 5a, the  $(\text{Na}_2\text{O})_{8.0}$  versus  $(\text{FeO})_{8.0}$  slope seems to become more negative with decreasing spreading rate. Thus, the model of Niu and Batiza [1993] cannot be used to explain the variation of the  $(\text{Na}_2\text{O})_{8.0}$  versus  $(\text{FeO})_{8.0}$  slope in terms of style of mantle upwelling. Langmuir et al. [1992] have shown that the EPR global and local trends overlap (negative correlation between  $(\text{Na}_2\text{O})_{8.0}$  and  $(\text{FeO})_{8.0}$ ), both being distinct

from the global vector and the Atlantic local vector. They ascribed this particular feature to melting of a mantle that is heterogeneous on a small scale (an enriched component is present in veins within a depleted matrix). The negative  $(\text{Na}_2\text{O})_{8.0}$  versus  $(\text{FeO})_{8.0}$  slope exhibited by PAR data is smaller than the global vector and could be explained by such a process.

**7.4.4. Geochemistry and axial depth.** Correlations between geochemistry and axial depth are quite weak along the PAR. This can be due to the weak variations of chemistry, to the rather flat along ridge bathymetric profile, or to both. A general relation which could be suggested here is that axial depth range, more than any other physical parameter, may control the first order geochemical variability. The positive correlation between extent of melting (inversely proportional to  $(\text{Na}_2\text{O})_{8.0}$ ) and axial depth is disconcerting (see Figure 5b). It has been shown [Géli et al., 1997] that a change in the geometry of the Pacific-Antarctic plates boundary has propagated southwestward for the last 30 to 35 Myr in response to the southwestward migration of the Euler pole of rotation. Because the area overlies a mantle with few thermal and compositional variations, it could be that the ridge topography is controlled more by plate dynamic constraints than by mantle temperature variations.

Vlastelic et al. [1999] have pointed out to a difference in average axial depth between the 25°S-20°N EPR and the southern Pacific ridges, suggesting a difference in thermal regime between the two mantles domains. However, the difference in mantle temperatures is not supported by the similarity in major element amounts (used in the temperature calculation) in the two areas (Table 2).

## 8. Conclusions

We have studied the geochemical characteristics of the Pacific-Antarctic Ridge between 56°S and 66°S. Our conclusions are based on the premise that although observed trends are defined by limited sampling; nevertheless, they reveal significant geochemical features of the underlying mantle. They can be summarized as follows:

1. Over a distance of 1800 km the Pacific-Antarctic Ridge (56-66°S) samples a homogeneous depleted mantle, which presents local geochemical variability. It contrasts with the PAR north of 56°S: Uditsev FZ appears as a limit between two regions, one to the north with large isotopic variation and one to the south where the isotopic variations are much more subdued.
2. The 56-66°S PAR samples have on average lower  $^{87}\text{Sr}/^{86}\text{Sr}$  and  $^{143}\text{Nd}/^{144}\text{Nd}$  and higher  $^{206}\text{Pb}/^{204}\text{Pb}$  than MORB from the 16°N-23°S EPR (and also than MORB from other oceans).
3. The relatively high variability of Pb isotopic ratios can be interpreted as the result of a general HIMU affinity of the southern Pacific upper mantle or in terms of a mantle event first recorded in time by Pb isotopes.
4. Mantle temperature displays few variations (30-40°C) along the 56-66°S PAR. Contrary to what is observed along the SEIR (88-118°E), PAR morphology appears to be controlled more by spreading rate rather than by mantle temperature.
5. Most of the observed major and trace element variations are related to ridge segmentation. Transform faults modify the shallowest thermal structure of the mantle and affect the top of the melting column. The cold edge is more effective in the axial dome context, resulting in an increase of the TFE magnitude along the valley-dome morphological transition.
6. There is no clear evidence for the speculated southwestward asthenospheric flow. However, this flow model could explain the observed intrasegment asymmetric patterns.

7. This regional study supports the idea that the bathymetry more than any other parameter such as spreading rate or ridge axis morphology is the main controlling factor of the first-order geochemical variability. This might apply to all mid-ocean ridges.

**Acknowledgments.** Helpful reviews were made by P. R. Castillo and D. M. Christie. We wish to thank H. Ondréas, J. L. Olivet, and A. Briais for fruitful discussions. We also thank Captain G. Tredunit and the crew of R/V L'Atalante for their efforts during the Pacantarctic cruise. This work benefited from financial support from Institut National des Sciences de l'Univers (INSU), IFREMER, and the DORSALES program.

## References

- Allègre, C.J., B. Hamelin, and B. Dupré, Statistical analysis of isotopic ratios in MORB: The mantle blob cluster model and convective regime of the mantle, *Earth Planet. Sci. Lett.*, **71**, 71-84, 1984.
- Bach, W., E. Hegner, J. Erzinger, and M. Satir, Chemical and isotopic variations along the superfast spreading East Pacific Rise from 6°S to 30°S, *Contrib. Mineral. Petrol.*, **116**, 365-380, 1994.
- Bach, W., J. Erzinger, L. Dosso, C. Bollinger, H. Bougault, J. Etoubleau, and J. Sauerwein, Unusually large Nb-Ta depletions in north Chile ridge basalts at 36° 50' to 38° 56'S: Major element, trace element, and isotopic data, *Earth Planet. Sci. Lett.*, **142**, 223-240, 1996.
- Batiza, R., Inverse relationship between Sr isotope diversity and rate of oceanic volcanism has implications for mantle heterogeneity, *Nature*, **309**, 440-441, 1984.
- Bender, J.F., and C.H. Langmuir, The Tamayo region of the EPR: Constraints on the TFE model from off-axis sampling, *Eos Trans. AGU*, **66**, 1108, 1985.
- Brown, J.W., and R.S. White, Variation with spreading rate of oceanic crustal thickness and geochemistry, *Earth Planet. Sci. Lett.*, **121**, 435-449, 1994.
- Castillo, P., and R. Batiza, Strontium, neodymium and lead isotope constraints on near-ridge seamount production beneath the South Atlantic, *Nature*, **342**, 262-265, 1989.
- Castillo, P.R., J. Natland, Y. Niu, and P.F. Lonsdale, Sr, Nd and Pb isotopic variation along the Pacific-Antarctic risecrest, 53-57°S: Implications for the composition and dynamics of the South Pacific upper mantle, *Earth Planet. Sci. Lett.*, **154**, 109-125, 1998.
- Chen, Y.C., and W.J. Morgan, Rift valley/no rift valley transition at mid ocean ridges, *J. Geophys. Res.*, **95**, 17,571-17,581, 1990a.
- Chen, Y.C., and W.J. Morgan, A nonlinear rheology model for mid-ocean ridge axis topography, *J. Geophys. Res.*, **95**, 17,583-17,604, 1990b.
- Cheng, Q., K.-H. Park, J.D. Macdougall, A. Zindler, G.W. Lugmair, H. Staudigel, J. Hawkins, and P. Lonsdale, Isotopic evidence for a hotspot origin of the Louisville Seamount Chain, in *Seamounts, Islands, and Atolls*, *Geophys. Monogr. Ser.*, vol. 43, edited by B.H. Keating et al., pp. 283-296, AGU, Washington, D.C., 1987.
- Church, S.E., and M. Tatsumoto, Lead isotope relations in oceanic ridge basalts from the Juan de Fuca-Gorda Ridge area, N.E. Pacific Ocean, *Contrib. Mineral. Petrol.*, **53**, 253-279, 1975.
- Cohen, R.S., and R.K. O'Nions, The lead, neodymium and strontium isotopic structure of ocean ridge basalts, *J. Petrol.*, **23**, 299-324, 1982.
- Cohen, R.S., N.M. Evensen, P.J. Hamilton, and R.K. O'Nions, U-Pb, Sm-Nd and Rb-Sr systematics of mid-ocean ridge basalt glasses, *Nature*, **283**, 149-153, 1980.
- DeMets, C., R.G. Gordon, D.F. Argus, and S. Stein, Current plate motions, *Geophys. J. R. Astron. Soc. London*, **101**, 425-478, 1990.
- Devey, C.W., C.D. Garbe-Schönberg, C. Stoffers, C. Chauvel, and D.F. Mertz, Geochemical effect of dynamic melting beneath ridges: Reconciling major and trace element variations in Kolbeinsey (and global) mid-ocean ridge basalt, *J. Geophys. Res.*, **99**, 9077-9095, 1994.
- Dickey, J.S., F.A. Frey, S.T. Hart, and E.B. Watson, Geochemistry and petrology of dredged basalts from the Bouvet triple junction, South Atlantic, *Geochim. Cosmochim. Acta*, **41**, 1105-1118, 1977.
- Dosso, L., H. Bougault, P. Beuzart, J.Y. Calvez, and J.L. Joron, The geochemical structure of the South-East Indian Ridge, *Earth Planet. Sci. Lett.*, **88**, 47-59, 1988.
- Dosso, L., B.B. Hanan, H. Bougault, J.G. Schilling, and J.L. Joron, Sr-Nd-Pb geochemical morphology between 10°N and 17°N on the Mid-Atlantic Ridge-A new MORB isotope signature, *Earth Planet. Sci. Lett.*, **106**, 29-43, 1991.
- Dosso, L., H. Bougault, and J.L. Joron, Geochemical morphology of the north Mid-Atlantic Ridge, 10°-24°N: Trace element-isotopes complementarity, *Earth Planet. Sci. Lett.*, **120**, 443-462, 1993.
- Dosso, L., H. Bougault, C.H. Langmuir, C. Bollinger, O. Bonnier, and J. Etoubleau, The age and distribution of mantle heterogeneity along the Mid-Atlantic Ridge (31-41°N), *Earth Planet. Sci. Lett.*, **170**, 269-286, 1999.
- Dupré, B., and C.J. Allègre, Pb-Sr-Nd isotopic correlation and the chemistry of the North Atlantic mantle, *Nature*, **286**, 17-22, 1980.
- Dupré, B., and C.J. Allègre, Pb-Sr isotope variation in Indian Ocean basalts and mixing phenomena, *Nature*, **303**, 142-146, 1983.
- Dupré, B., B. Lambret, D. Rousseau, and C.J. Allègre, Limitations on the scale of mantle heterogeneities under oceanic ridges, *Nature*, **294**, 552-554, 1981.
- Ferguson, E.M., and E.M. Klein, Fresh basalts from the Pacific Antarctic Ridge extend the Pacific geochemical province, *Nature*, **366**, 330-333, 1993.
- Fontignie, D., and J.G. Schilling, <sup>87</sup>Sr/<sup>86</sup>Sr and REE variations along the Easter Microplate boundaries (South Pacific): Application of multivariate statistical analysis to ridge segmentation, *Chem. Geol.*, **89**, 209-241, 1991.
- Fontignie, D., and J.G. Schilling, Mantle heterogeneities beneath the South Atlantic: A Nd-Sr-Pb isotope study along the Mid-Atlantic Ridge (3°S-46°S), *Earth Planet. Sci. Lett.*, **142**, 209-221, 1996.
- Frey, F.A., N. Walker, D. Stakes, S.R. Hart, and R. Nielsen, Geochemical characteristics of basaltic glasses from the Amar and Famous axial valleys, Mid-Atlantic Ridge (36°-37°N)-Petrogenetic implications, *Earth Planet. Sci. Lett.*, **115**, 117-136, 1993.
- Géli, L., et al., Evolution of the Pacific-Antarctic Ridge south of the Uditsev fracture zone, *Science*, **278**, 1281-1284, 1997.
- Géli, L., D. Aslanian, J.L. Olivet, I. Vlastelic, L. Dosso, H. Guillou, and H. Bougault, Location of Louisville Hotspot and origin of Hollister ridge: Geophysical constraints, *Earth Planet. Sci. Lett.*, **164**, 31-40, 1998.
- Graham, D.W., P.R. Castillo, J.E. Lupton, and R. Batiza, Correlated He and Sr isotope ratios in South Atlantic near-ridge seamounts and implications for mantle dynamics, *Earth Planet. Sci. Lett.*, **144**, 491-503, 1996.
- Green, T.H., Petrology and geochemistry of basaltic rocks from the Balleny Islands, Antarctica, *Aust. J. Earth Sci.*, **39**, 603-617, 1992.
- Gurenko, A., and M. Chaussidon, Enriched and depleted primitive melts included in olivine from Icelandic tholeites: Origin by continuous melting of a single mantle column, *Geochim. Cosmochim. Acta*, **59**, 2905-2917, 1995.
- Hamelin, B., and C.J. Allègre, Large-scale regional units in the depleted upper mantle revealed by an isotope study of the South-West Indian Ridge, *Nature*, **315**, 196-199, 1985.
- Hamelin, B., B. Dupré, and C.J. Allègre, Lead-strontium isotopic variations along the East Pacific Rise and the Mid-Atlantic Ridge: A comparative study, *Earth Planet. Sci. Lett.*, **67**, 340-350, 1984.
- Hamelin, B., B. Dupré, and C.J. Allègre, Pb-Sr-Nd isotopic data of Indian Ocean ridges: New evidence of large-scale mapping of mantle heterogeneities, *Earth Planet. Sci. Lett.*, **76**, 288-298, 1986.
- Hanan, B.B., and J.G. Schilling, Easter microplate evolution: Pb isotope evidence, *J. Geophys. Res.*, **94**, 7432-7448, 1989.
- Hanan, B.B., R.H. Kingsley, and J.-G. Schilling, Pb isotope evidence in the South Atlantic for migrating ridge-hotspot interactions, *Nature*, **322**, 137-144, 1986.
- Hart, S.R., J.G. Schilling, and J.L. Powell, Basalts from Iceland and along the Reykjanes Ridge: Sr isotope geochemistry, *Nature*, **246**, 104-107, 1973.
- Hegner, E., and M. Tatsumoto, Pb, Sr, and Nd isotopes in basalts and sulfides from the Juan de Fuca Ridge, *J. Geophys. Res.*, **92**, 11,380-11,386, 1987.
- Hémond, C., and C.W. Devey, The Foundation Seamount Chain, southeastern Pacific: First isotopic evidence of a newly discovered hotspot track, *J. Conf. Abstr.*, **1** (1) 255, 1996.
- Hofmann, A.W., Chemical differentiation of the Earth: The relationship between mantle, continental, and oceanic crust, *Earth Planet. Sci. Lett.*, **90**, 297-314, 1988.
- Ito, E., W.M. White, and C. Göpel, The O, Sr, Nd and Pb isotope geochemistry of MORB, *Chem. Geol.*, **62**, 157-176, 1987.
- Johnson, K.T.M., H.J.B. Dicks, and N. Shimizu, Melting in the oceanic upper mantle: An ion microprobe study of diopside in abyssal peridotites, *J. Geophys. Res.*, **95**, 2661-2678, 1990.

- Klein, E., and C.H. Langmuir, Global correlations of ocean ridge basalt chemistry with axial depth and crustal thickness, *J. Geophys. Res.*, 92, 8089-8115, 1987.
- Klein, E.M., and C.H. Langmuir, Local versus global variations in ocean ridge basalt composition: A reply, *J. Geophys. Res.*, 94, 4241-4252, 1989.
- Klein, E.M., C.H. Langmuir, A. Zindler, H. Staudigel, and B. Hamelin, Isotope evidence of a mantle convection boundary at the Australian-Antarctic discordance, *Nature*, 333, 623-629, 1988.
- Kurz, M.D., A.P. Le Roex, and H.J.B. Dick, Isotope geochemistry of the oceanic mantle near the Bouvet triple junction, *Geochim. Cosmochim. Acta*, 62, 841-852, 1998.
- Langmuir, C.H., and J.F. Bender, The geochemistry of oceanic basalts in the vicinity of transform faults: Observations and implications, *Earth Planet. Sci. Lett.*, 69, 107-127, 1984.
- Langmuir, C.H., E.M. Klein, and T. Plank, Petrological systematics of mid-ocean ridge basalts: constraints on melt generation beneath ocean ridges, in *Mantle Flow and Melt Generation at Mid-Ocean Ridges, Geophys. Monogr. Ser.*, vol 71, edited by J. Phipps Morgan, D.K. Blackman and J. M. Sinton, pp. 183-280, AGU, Washington, D.C., 1992.
- Lanyon, R., R. Varne, and A.J. Crawford, Tasmanian Tertiary basalts, the Balleny Plume, and opening of the Tasman Sea (southwest Pacific Ocean), *Geology*, 21, 555-558, 1993.
- Le Roex, A.P., H.J.B. Dick, A.J. Erlank, A.M. Reid, F.A. Frey, and S.R. Hart, Geochemistry, mineralogy and petrogenesis of lavas erupted along the Southwest Indian Ridge between the Bouvet Triple Junction and 11°East, *J. Petrol.*, 24, 267-318, 1983.
- Le Roex, A.P., H.J.B. Dick, A.M. Reid, F.A. Frey, A.J. Erlank, and S.R. Hart, Petrology and geochemistry of basalts from the American-Antarctic Ridge, Southern Ocean: Implications for the westward influence of the Bouvet mantle plume, *Contrib. Mineral. Petrol.*, 90, 367-380, 1985.
- Le Roex, A.P., H.J.B. Dick, L. Gulen, A.M. Reid, and A.J. Erlank, Local and regional heterogeneity in MORB from the Mid-Atlantic Ridge between 54°S and 51°S: Evidence for geochemical enrichment, *Geochim. Cosmochim. Acta*, 51, 541-555, 1987.
- Le Roex, A.P., H.J.B. Dick, and R.T. Watkins, Petrogenesis of anomalous K-enriched MORB from the Southwest Indian Ridge: 11°53'E to 14°38'E, *Contrib. Mineral. Petrol.*, 110, 253-268, 1992.
- Lonsdale, P., Geomorphology and structural segmentation of the crest of the southern (Pacific-Antarctic) East Pacific Rise, *J. Geophys. Res.*, 99, 4683-4702, 1994.
- Macdougall, J.D., and G.W. Lugmair, Extreme isotopic homogeneity among basalts from the southern East Pacific Rise: Mantle or mixing effect?, *Nature*, 313, 209-211, 1985.
- Macdougall, J.D., and G.W. Lugmair, Sr and Nd isotopes in basalts from the East Pacific Rise: Significance for mantle heterogeneity, *Earth Planet. Sci. Lett.*, 77, 273-284, 1986.
- Machado, N., J.N. Ludden, C. Brooks, and G. Thompson, Fine scale isotopic heterogeneity in the sub-Atlantic mantle, *Nature*, 295, 226-228, 1982.
- Mahoney, J.J., J.H. Natland, W.M. White, R. Poreda, S.H. Bloomer, R.L. Fisher, and A.N. Baxter, Isotopic and geochemical provinces of the western Indian ocean spreading centers, *J. Geophys. Res.*, 94, 4033-4052, 1989.
- Mahoney, J., A.P. Leroex, Z. Peng, R.L. Fisher, and J.H. Natland, Southwestern limits of Indian Ocean ridge mantle and the origin of low  $^{206}\text{Pb}/^{204}\text{Pb}$  mid-ocean ridge basalt-isotope systematics of the central Southwest Indian Ridge (17°E-50°E), *J. Geophys. Res.*, 97, 19,771-19,790, 1992.
- Mahoney, J.J., J.M. Sinton, M.D. Kurz, J.D. Macdougall, K.J. Spencer, and G.W. Lugmair, Isotope and trace element characteristics of a super-fast spreading ridge: East Pacific Rise, 13-23°S, *Earth Planet. Sci. Lett.*, 121, 173-193, 1994.
- Marks, K.M., and J.M. Stock, Variations in Ridge Morphology and Depth-Age Relationships on the Pacific-Antarctic Ridge, *J. Geophys. Res.*, 99, 531-541, 1994.
- McKenzie, D., The extraction of magma from the crust and mantle, *Earth Planet. Sci. Lett.*, 74, 81-91, 1985.
- Mertz, D.F., and K.M. Haase, The radiogenic isotope composition of the high-latitude North Atlantic mantle, *Geology*, 25, 411-414, 1997.
- Mertz, D.F., C.W. Devey, W. Todt, P. Stoffers, and A.W. Hofmann, Sr-Nd-Pb isotope evidence against plume asthenosphere mixing north of Iceland, *Earth Planet. Sci. Lett.*, 107, 243-255, 1991.
- Michard, A., R. Montigny, and R. Schlich, Geochemistry of the mantle beneath the Rodriguez Triple Junction and the South-East Indian Ridge, *Earth Planet. Sci. Lett.*, 78, 104-114, 1986.
- Niu, Y., Mid-ocean ridge magmatism: Style of mantle upwelling, partial melting, crustal level processes, and spreading rate dependence: A petrologic approach, Ph.D. thesis, 250 pp., Univ. of Hawaii, Honolulu, 1992.
- Niu, Y., and R. Batiza, An empirical method for calculating melt compositions produced beneath mid-ocean ridges: Application for axis and off-axis (seamounts) melting, *J. Geophys. Res.*, 96, 21,753-21,777, 1991.
- Niu, Y., and R. Batiza, Chemical variation trends at fast and slow spreading mid-ocean ridges, *J. Geophys. Res.*, 98, 7887-7902, 1993.
- Niu, Y., and R. Batiza, Magmatic processes at slow spreading ridge segment: 26°S Mid-Atlantic Ridge, *J. Geophys. Res.*, 99, 19,719-19,740, 1994.
- Niu, Y., and R. Hekinian, Spreading-rate dependence of the extend of mantle melting beneath ocean ridges, *Nature*, 385, 326-329, 1997.
- Niu, Y., D.G. Waggoner, J.M. Sinton, and J.J. Mahoney, Mantle source heterogeneity and melting processes beneath seafloor spreading centers: The East Pacific Rise, 18°-19°S, *J. Geophys. Res.*, 101, 27,711-27,733, 1996.
- Niu, Y.L., K.D. Collerson, R. Batiza, J.I. Wendt, and M. Regelous, Origin of enriched-type mid-ocean ridge far from mantle plumes: The East Pacific Rise at 11°20'N, *J. Geophys. Res.*, 104, 7067-7087, 1999.
- Phipps Morgan, J., and Y.J. Chen, Dependence of ridge-axis morphology on magma supply and spreading rate, *Nature*, 364, 706-708, 1993.
- Phipps Morgan, J., and D.W. Forsyth, Three-dimensional flow and temperature perturbations due to a transform offset: Effects on oceanic crustal and upper mantle structure, *J. Geophys. Res.*, 93, 2955-2966, 1988.
- Phipps Morgan, J., E.M. Parmentier, and J. Lin, Mechanisms for the origin of mid-ocean ridge axial topography: Implication for the thermal and mechanical structure of accreting plate boundaries, *J. Geophys. Res.*, 92, 12,823-12836, 1987.
- Plank, T., and C.H. Langmuir, Effects of the melting regime on the composition of the oceanic crust, *J. Geophys. Res.*, 97, 19,749-19,770, 1992.
- Price, R.C., A.K. Kennedy, M. Riggs-Sneeringer, and F.A. Frey, Geochemistry of basalts from the Indian Ocean triple junction: Implications for the generation and evolution of Indian Ocean Ridge basalts, *Earth Planet. Sci. Lett.*, 78, 379-396, 1986.
- Prinzhofer, A., E. Lewin, and C.J. Allègre, Stochastic melting of the marble cake mantle: Evidence from local study of the East Pacific Rise at 12°50'N, *Earth Planet. Sci. Lett.*, 92, 189-206, 1989.
- Pyle, D.G., D.M. Christie, and J.J. Mahoney, Resolving an isotopic boundary within the Australian-Antarctic Discordance, *Earth Planet. Sci. Lett.*, 112, 161-178, 1992.
- Roult, G., D. Rouland, and J.P. Montagner, Antarctica II: Upper mantle structure from velocities and anisotropy, *Phys. Earth Planet. Inter.*, 84, 33-57, 1994.
- Sahabi, M., L. Géli, J.L. Olivet, L. Gilgcapar, G. Roult, H. Ondreas, P. Beuzart, and D. Aslanian, Morphological reorganization within the Pacific-Antarctic discordance, *Earth Planet. Sci. Lett.*, 137, 157-173, 1996.
- Sandwell, D.T., W.H.F. Smith, and M.M. Yale, ERS-1 geodetic mission reveals detailed tectonic structures, *Eos Trans. AGU*, 75(44), Fall Meet. Suppl., 155, 1994.
- Schiano, P., J.L. Birck, and C.J. Allègre, Osmium-strontium-neodymium-lead isotopic covariations in mid-ocean ridge basalt glasses and the heterogeneity of the upper mantle, *Earth Planet. Sci. Lett.*, 150, 363-379, 1997.
- Schilling, J.G., Iceland mantle plumes: Geochemical evidence along the Reykjanes Ridge, *Nature*, 242, 565-571, 1973.
- Schilling, J.G., B.B. Hanan, B. McCullly, R.H. Kingsley, and D. Fontignie, Influence of the Sierra Leone mantle plume on the equatorial Mid-Atlantic Ridge: A Nd-Sr-Pb isotopic study, *J. Geophys. Res.*, 99, 12,005-12,028, 1994.
- Schilling, J.G., C. Ruppel, A.N. Davis, B. McCullly, S.A. Tighe, R.H. Kingsley, and J. Lin, Thermal structure of the mantle beneath the equatorial Mid-Atlantic Ridge: Inferences from the spatial variation of dredged basalt glass compositions, *J. Geophys. Res.*, 100, 10,057-10,076, 1995.
- Shah, A.K., and J.C. Sempére, Morphology of the transition from an axial high to a rift valley at the Southeast Indian Ridge and the relation to variations in mantle temperature, *J. Geophys. Res.*, 103, 5203-5223, 1998.
- Shaw, D.M., Trace element fractionation during anatexis, *Geochim. Cosmochim. Acta*, 34, 237-243, 1970.

- Shen, Y., and D.W. Forsyth, Geochemical constraints on initial and final depths of melting beneath mid-ocean ridges, *J. Geophys. Res.*, **100**, 2211-2237, 1995.
- Shirey, S.B., J.F. Bender, and C.H. Langmuir, Three-component isotopic heterogeneity near the Oceanographer transform Mid-Atlantic Ridge, *Nature*, **325**, 217-223, 1987.
- Sinton, J.M., S.M. Smaglik, J.J. Mahoney, and K.C. McDonald, Magmatic processes at superfast mid-ocean ridges: Glass compositional variations along the East Pacific Rise 13°-23°S, *J. Geophys. Res.*, **96**, 6133-6155, 1991.
- Sleep, N., Tapping of magmas from ubiquitous mantle heterogeneities: An alternative to mantle plume?, *J. Geophys. Res.*, **89**, 10,029-10,041, 1984.
- Sleep, N.H., Tapping of melt by veins and dykes, *J. Geophys. Res.*, **93**, 10,255-10,272, 1988.
- Small, C., and D.T. Sandwell, An abrupt change in ridge axis gravity with spreading rate, *J. Geophys. Res.*, **94**, 17,383-17,392, 1989.
- Smith, W.H.F., and D.T. Sandwell, Global sea floor topography from satellite altimetry and ship depth soundings, *Science*, **277**, 1956-1962, 1997.
- Sun, W., C.Z. Mutter, J.C. Mutter, and W.R. Buck, Some theoretical predictions on the relationships among spreading rate, mantle temperature, and crustal thickness, *J. Geophys. Res.*, **99**, 3215-3227, 1994.
- Sun, S.S., Lead isotopic study of young volcanic rocks from mid-ocean ridges, ocean islands and island arcs, *Philos. Trans. R. Soc. London, Ser. A*, **297**, 409-445, 1980.
- Sun, S.S., M. Tatsumoto, and J.G. Schilling, Mantle plume mixing along the Reykjanes ridge axis: Lead isotopic evidence, *Science*, **190**, 143-147, 1975.
- Sun, S.S., R.W. Nesbitt, and A.E. Sharaskin, Geochemical characteristics of mid-ocean ridge basalts, *Earth Planet. Sci. Lett.*, **44**, 119-138, 1979.
- Tatsumoto, M., Isotopic composition of lead in oceanic basalt and its implication to mantle evolution, *Earth Planet. Sci. Lett.*, **38**, 63-87, 1978.
- Verma, S.P., J.G. Schilling, and D.G. Waggoner, Neodynium isotopic evidence for Galapagos hotspot-spreading centre system evolution, *Nature*, **306**, 654-657, 1983.
- Vidal, P., and N. Clauer, Pb and Sr isotopic systematics of some basalts and sulfides from the East Pacific Rise at 21°N (project RITA), *Earth Planet. Sci. Lett.*, **55**, 237-246, 1981.
- Vlastelic, I., L. Dosso, H. Bougault, L. Géli, J. Etoubleau, and J.L. Joron, Geochemistry of the Hollister Ridge: Relation with the Louisville hotspot and the Pacific-Antarctic Ridge, *Earth Planet. Sci. Lett.*, **160**, 777-793, 1998.
- Vlastelic, I., D. Aslanian, L. Dosso, H. Bougault, J.L. Olivet, and L. Géli, Large-scale chemical and thermal division of the Pacific mantle, *Nature*, **399**, 345-350, 1999.
- Vogt, P., and G.L. Johnson, Transform faults and longitudinal flow below the mid-oceanic ridge, *J. Geophys. Res.*, **80**, 1399-1427, 1975.
- White, W.M., and A.W. Hofmann, Sr and Nd isotope geochemistry of oceanic basalts and mantle evolution, *Nature*, **296**, 821-825, 1982.
- White, W.M., and J.G. Schilling, The nature and origin of geochemical variation in Mid-Atlantic Ridge basalts from the central North Atlantic, *Geochim. Cosmochim. Acta*, **42**, 1501-1516, 1978.
- White, W.M., A.W. Hofmann, and H. Puchelt, Isotope geochemistry of Pacific mid-ocean ridge basalt, *J. Geophys. Res.*, **92**, 4881-4893, 1987.
- Yu, D., D. Fontignie, and J.-G. Schilling, Mantle plume-ridge interactions in the central North Atlantic: A Nd isotope study of Mid-Atlantic Ridge basalts from 30°N to 50°N, *Earth Planet. Sci. Lett.*, **146**, 259-272, 1997.
- Zindler, A., H. Staudigel, and R. Batiza, Isotope and trace element geochemistry of young Pacific Seamounts: Implications for the scale of upper mantle heterogeneity, *Earth Planet. Sci. Lett.*, **70**, 175-195, 1984.

D. Aslanian, H. Bougault, J. Etoubleau, and L. Géli, IFREMER, B.P. 70, F-29280 Plouzané, France.

M. Bohn, C. Bollinger, and L. Dosso, UMR 6538, Domaines océaniques, IFREMER, B.P. 70, F-29280 Plouzané, France. (Laure.Dosso@ifremer.fr)

J.-L. Joron, Groupe des sciences de la Terre, Laboratoire Pierre Süe, Centre d'Etude Nucléaire de Saclay, B.P. 2, Gif sur Yvette, France.

I. Vlastelic, Max Planck-Institut für chemie, Abteilung Geochemie, Postfach 3060, D-55020 Mainz, Germany.

(Received October 28, 1998, revised June 10, 1999; accepted June 23, 1999.)